Melt Generation and Evolution of Magmatic Systems in Extensional Settings on Venus: A Semi-Analytical Modeling Approach

by

Rudi Renee Lien

A thesis accepted and approved in partial fulfillment of the

requirements for the degree of

Master of Science

in Earth Sciences

Thesis Committee:

Josef Dufek, Chair

Katharine V. Cashman, Member

Meredith Townsend, Member

Kathleen Craft, Member

University of Oregon

Spring 2024

THESIS ABSTRACT

Rudi Renee Lien

Master of Science in Earth Sciences

Title: Melt Generation and Evolution of Magmatic Systems in Extensional Settings on Venus: A Semi-Analytical Modeling Approach

The planet Venus appears to be the only geologically active planet in the solar system at present, aside from Earth. This long-sustained activity is reflected by globally distributed tectonic and volcanic features and evidence for ongoing volcanism. Here, I investigate magma production in the interior of Venus to better understand what thermal conditions are required to source active volcano-tectonic interactions. I developed a two-dimensional semi-analytical model to quantify melt production rates and the thermal evolution of the Venusian interior due to thinning of the lithosphere. Results indicate that large-scale melting (10^{-5}–10^{-2} $m^3/m^2/yr$) is possible under present-day Venusian conditions for a broad range of parameters, although the melt production rates are consistently lower (by at least one order of magnitude) than those at similar geologic settings on Earth. This work characterizes the interior processes that may drive magmatism, volcanism, and tectonism on Venus, which has greater implications for planet evolution.

This thesis includes unpublished co-authored material.

ACKNOWLEDGMENTS

I would like to thank my advisor, Dr. Joe Dufek, for supporting this research in the form of in-depth discussions on my research ideas, methodologies, and outcomes over the last three years. Additional thanks are due to my committee members – Drs. Kathy Cashman, Meredith Townsend, and Kate Craft – for their constructive feedback on this research thesis and my progress during my time at the University of Oregon. This work was supported by NASA and Oregon Space Grant Consortium (OSGC), cooperative agreement 80NSSC20M0035.

TABLE OF CONTENTS

Chapter Page

LIST OF FIGURES

LIST OF TABLES

Table Page

CHAPTER 1.

INTRODUCTION

The planet Venus is often referred to as Earth's sister planet due to its similarities in planetary radius, distance from the Sun, and bulk density, which indicates similar interior structure and composition (e.g., Margot et al., 2021; Smrekar et al., 2018). Despite these Earth-like qualities, Venus experienced a runaway greenhouse effect at some point in its past that caused global loss of water (from surface and shallow subsurface reservoirs) and the growth of a dense, carbon dioxide-rich atmosphere (e.g., Ingersoll, 1969; Kasting, 1988). At present, the Venusian atmosphere allows for average surface temperature and pressure of ~475 °C and 9.20 MPa, respectively, making the surface an extreme and uninhabitable environment that is challenging to explore and study. Because Venus had the potential to maintain surface water and habitable conditions, or possibly even resembled Earth earlier in its evolution, it is important to understand why the evolution of these two planets diverged so significantly. The tectonic and volcanic processes that are active on Venus, or were active in the past, can provide insights into generation and recycling of the crust as well as transport of volatiles between the interior and atmosphere, all of which are potential contributors to the divergence of Venus and Earth. The work presented here focuses on identifying the conditions required to generate melt in the Venusian interior at present or in the recent past, which are necessary to understand melt availability, crustal generation, volatile transport, and the types of volcanic processes to expect. Chapters 1-4 within this thesis will be published as one journal article with co-author Dr. Josef Dufek.

1.1. Thermal State of the Interior and Geodynamic Regime(s)

The thermal state and heat transport mechanisms of a planetary body are primary controls on geologic activity and the associated features that can be observed at the surface. The core-mantle boundary and the lithosphere-asthenosphere boundary are the thermal boundary layers within a planetary interior (Bercovici, 2010; Mulyukova and Bercovici, 2020; Schubert, 1997). The core is the primary heat source in a planetary body, while heat is either removed or insulated by the solid lithosphere. Heat from the core (and from radiogenic nuclides within the body) is transferred between these boundary layers via mantle convection (e.g., Bercovici, 2010; Mulyukova and Bercovici, 2020; Schubert, 1997). Heat transfer through the lithosphere is typically conductive and dependent on many factors, including lithosphere thickness, composition, and rheology, and volcanic or tectonic activity that weakens or fragments the lithosphere (e.g., Solomon and Head, 1982). Additionally, melt generation, magma accumulation, and volcanism efficiently transfer and remove heat (e.g. Nakagawa and Tackley, 2012), but these processes are ultimately controlled by the thermal state of the mantle asthenosphere. Therefore, mantle convection is the dominant control on the mechanism and rates of heat transport in a planetary interior as well as the geodynamic (or tectonic) regime. The spatial and temporal scales of mantle convection are reflected in the observable tectonic and magmatic/volcanic processes at a planet's surface, so in the case of Venus, direct observations from missions, laboratory experiments, and computational modeling have helped to constrain the present-day thermal state and geodynamic regime.

The active geodynamic regime on Venus has direct implications for global heat transfer and magmatic processes. While the geodynamic regime operating on Venus is widely debated, available observations may support a stagnant lid (e.g., Solomatov and Moresi, 1996), episodic

lid (e.g., Romeo and Turcotte, 2010; Strom et al., 1994), or plutonic-squishy lid regime (e.g., Byrne et al., 2021**;** Lourenço et al., 2020; Figure 1). A stagnant lid regime is characterized by a rigid, conductive lid (single plate) that is decoupled from the convecting mantle, which results in low surface heat flux and minimal to no horizontal movement or break up of lithospheric plates (e.g., Rolf et al., 2022; Solomatov and Moresi, 1996**;** Figure 1a). Despite the lack of plate break up or motion, volcanic activity is possible in the stagnant lid regime and likely sourced by mantle plumes. While most available evidence points to Venus being in a stagnant lid state at present, the surface of Venus displays numerous geologic features that suggest recent or ongoing tectonic and magmatic activity. This recent or ongoing activity implies that Venus deviates from a purely stagnant lid regime, unlike the other terrestrial bodies in the inner solar system (the Moon, Mars, and Mercury).

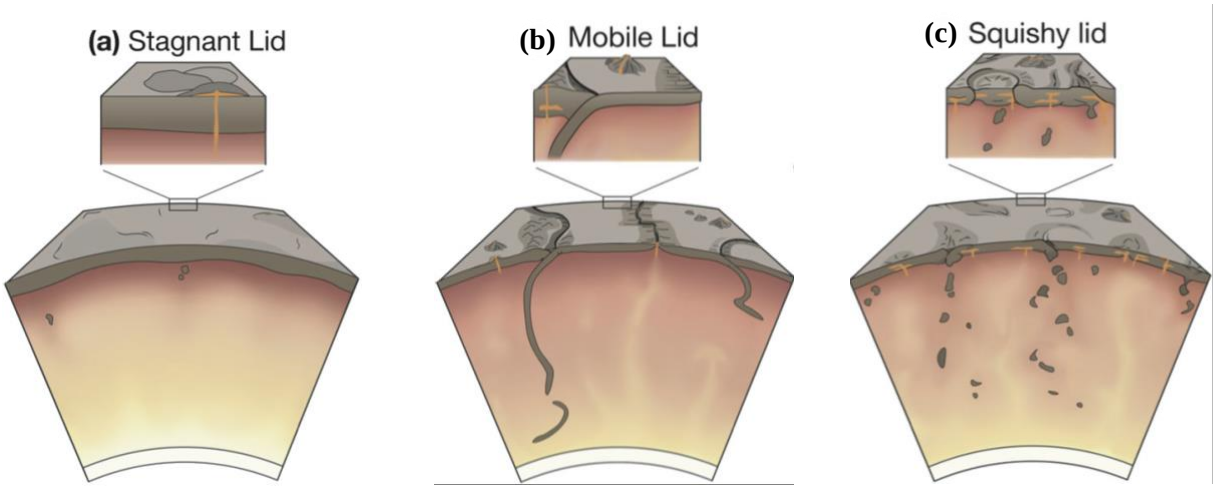

Figure 1. Depictions of proposed geodynamic regimes for Venus: (a) stagnant lid regime characterized by a rigid and conductive single plate lid with minimal to no horizontal movement or deformation; (b) mobile lid regime characterized by large, mobile plates and tectonically-driven crust generation and recycling mechanisms; and (c) plutonic-squishy lid regime characterized by substantial melt in the interior that thins and weakens the lithosphere and potentially fragments the lithosphere into small plates. Figure from Rolf et al., 2022.

Continued work on this topic suggests that Venus may be in a hybrid regime that falls between the mobile lid (Earth-like plate tectonics; Figure 1b) and stagnant lid regimes, such as the episodic lid or the plutonic-squishy lid regime. A conductive stagnant lid traps heat inside a body, and if the body is still warm enough so that mantle convection can occur or plumes are present, the trapped heat can cause melting in the asthenosphere. In the episodic lid regime, a planet experiences periodic overturn events characterized by high-volume volcanic activity, causing regional to global resurfacing (Strom et al., 1994). The overturn events are hypothesized to result from lithosphere (lid) destabilization caused by mantle plumes, which elevate interior temperatures, produce large volumes of melt in the asthenosphere, and apply stress to the overlying lithosphere. Post-overturn, the lid returns to longer periods of quiescence that resemble a stagnant lid state. Present-day eruption/resurfacing rate estimates based on crater distributions and cross-cutting relationships do not support the hypothesis of Venus being in an ongoing resurfacing episode (e.g., Bjonnes et al., 2012; Phillips et al., 1992; Rolf et al., 2022), although surface observations of Venus are minimal and at low resolutions. Additionally, it is challenging to distinguish a long-lasting stagnant state of an episodic lid regime and a purely stagnant lid regime, as both would show similar surface features, interior structure, and thermal properties. Lastly, the plutonic-squishy lid regime considers the effects of intrusive magmatism on a stagnant lid (Lourenço et al., 2018, 2020; Figure 1c). If substantial amounts of melt can intrude into the lithosphere, forming intrusive plutons, the lithospheric lid would be warmed and weakened regionally and may even fragment into small plates. The plutonic-squishy lid is characterized by a thin lithosphere, low eruption rates, localized deformation, and small, mobile plates, which may match some regions of Venus well. While both the episodic and plutonic-squishy lid regimes are dependent on high melt volumes in the interior, the majority of magmatic

activity is intrusive for the plutonic-squishy lid regime (>70%; Lourenço et al., 2020), in sharp contrast to the large eruptive volumes required for the episodic lid regime.

1.2. Volcano-Tectonic Interactions on Venus

Surface features such as wrinkle ridges and large rift systems are indicators of both compressional and extensional tectonic activity on Venus (Solomon et al., 1992; Figure 2a). Many sources indicate that decompression melting via mantle upwellings or plumes drive volcanism and potentially tectonic processes on Venus (e.g. Smrekar et al., 2010; Ivanov and Head, 2010; Gülcher et al., 2020). Age constraints are limited for the surface of Venus, but analysis of crater densities and cross-cutting relationships indicate that rifting and rift-associated volcanism have dominated the most recent geologic period, since the hypothesized global resurfacing event ~150-500 million years ago (Herrick and Rumpf, 2011; Ivanov and Head, 2013; Le Feuvre and Wieczorek, 2011; Strom et al., 1994). Additionally, some evidence suggests rifts in Atla Regio may have been active as recently as ≤50 million years ago (Basilevsky, 1993), and at present, rift systems span up to 40,000 km in length on Venus (Masursky et al., 1980; Schaber, 1982). Due to the prominence of rift activity in the recent past, we focus only on extensional processes in this work. As discussed in the previous section, these geologically young features suggest that Venus is not in a purely stagnant-lid regime. Multiple driving mechanisms for extensional tectonics have been proposed for Venus that are viable under stagnant-lid or plutonic-squishy lid conditions: mantle convection (Phillips, 1990); plume-driven extension (Airey et al., 2017); and lithospheric delamination/lid recycling (Turcotte, 1989; Elkins-Tanton et al., 2007; Ghail, 2015). While this work is not focused on defining the driving mechanism for extension, these mechanisms are related to the parameters considered in this work

(described in Section 2; Table 1), so our results may provide implications for which driving mechanism fits best with current and future observations.

1.3. Observations of Active Volcanism

More than 85,000 volcanic edifices have been identified across the surface of Venus (Hahn and Byrne, 2023; Figure 2b). Observations from NASA's Magellan and the European Space Agency (ESA) Venus Express Mission provided evidence for recent to present-day volcanism at rift systems and rift-associated shield volcanoes and coronae (e.g. Smrekar et al., 2010; Shalygin et al., 2015). Idunn Mons (46° S, 146° W) is a large shield volcano (200 km diameter) near the axis of the rift zone Olapa Chasma. Emissivity data from the Venus Express Mission provided evidence for chemically unweathered basalt at Idunn Mons, which is indicative of recent lava flows (Smrekar et al., 2010). Geochemical modeling and experiments performed under Venus' atmospheric conditions helped to constrain the possible age of the hypothesized lava flows at Idunn Mons to $10^1 – 10^4$ years (Cutler et al., 2020; Filiberto et al., 2020; D'Incecco et al., 2021). Surface mapping and cross-cutting relationships of lava flows and rift-associated fractures indicate that Idunn Mons and Olapa Chasma formed and evolved contemporaneously, likely developing a volcano-tectonic feedback (D'Incecco et al., 2020; López et al., 2022).

Atla Regio is a region of Venus that may contain multiple active volcanoes at present. At the Ganis Chasma rift zone, relative brightness in images taken by the Venus Monitoring Camera (VMC) on Venus Express was interpreted to represent changes in thermal emission and elevated surface temperatures (Basilevsky et al., 2012; Shalygin et al., 2015). The surface temperatures were quantified for multiple orbits in June 2008, and results showed that surface temperatures were temporarily elevated up to 1,100 K. VMC imagery from an orbit ~111 Earth days later indicated that surface temperatures had decreased to the average surface temperature, ~740 K, in

the areas where temperatures were previously elevated. This dramatic change in relative brightness and interpreted surface temperature is a strong indicator for an effusive volcanic eruption along the Ganis Chasma rift. A separate study (Herrick and Hensley, 2023) compared radar images taken by the Magellan mission (operating from 1990-1992) to look for any surface changes (e.g., ground deformation, lava flows, fractures) that may be indicative of volcanic activity that occurred during the mission. The Magellan images and follow-on stereo radargrammetry for topography analysis showed a vent on the Maat Mons volcano in Atla Regio that changed shape and expanded (nearly doubling in area) in the eight months between the two orbits over this location. This expansion was attributed to subsurface magmatic activity – either a new magmatic intrusion, which can expand a vent, or the draining of a magma chamber, which can cause a vent to collapse (Herrick and Hensley, 2023).

While coronae – quasi-circular volcano-tectonic features – are not a main focus of the work presented here, these features are often in close proximity to rift systems and also believed to form by mantle upwelling on Venus (e.g. Gerya, 2014; Roberts & Head, 1993), so we include a brief overview of their activity at present as well. Numerical modeling by Gülcher et al., 2020 suggest that coronae morphology can be indicative of recent or ongoing plume activity and associated volcanism, and they identified 37 active coronae based on their morphological analysis (Figure 2c). Lithospheric flexure models also indicate that the elastic lithosphere is locally thin and surface heat flux is elevated at some of these potentially active coronae (O'Rourke & Smrekar, 2018), supporting the hypothesis of ongoing plume or mantle upwelling activity.

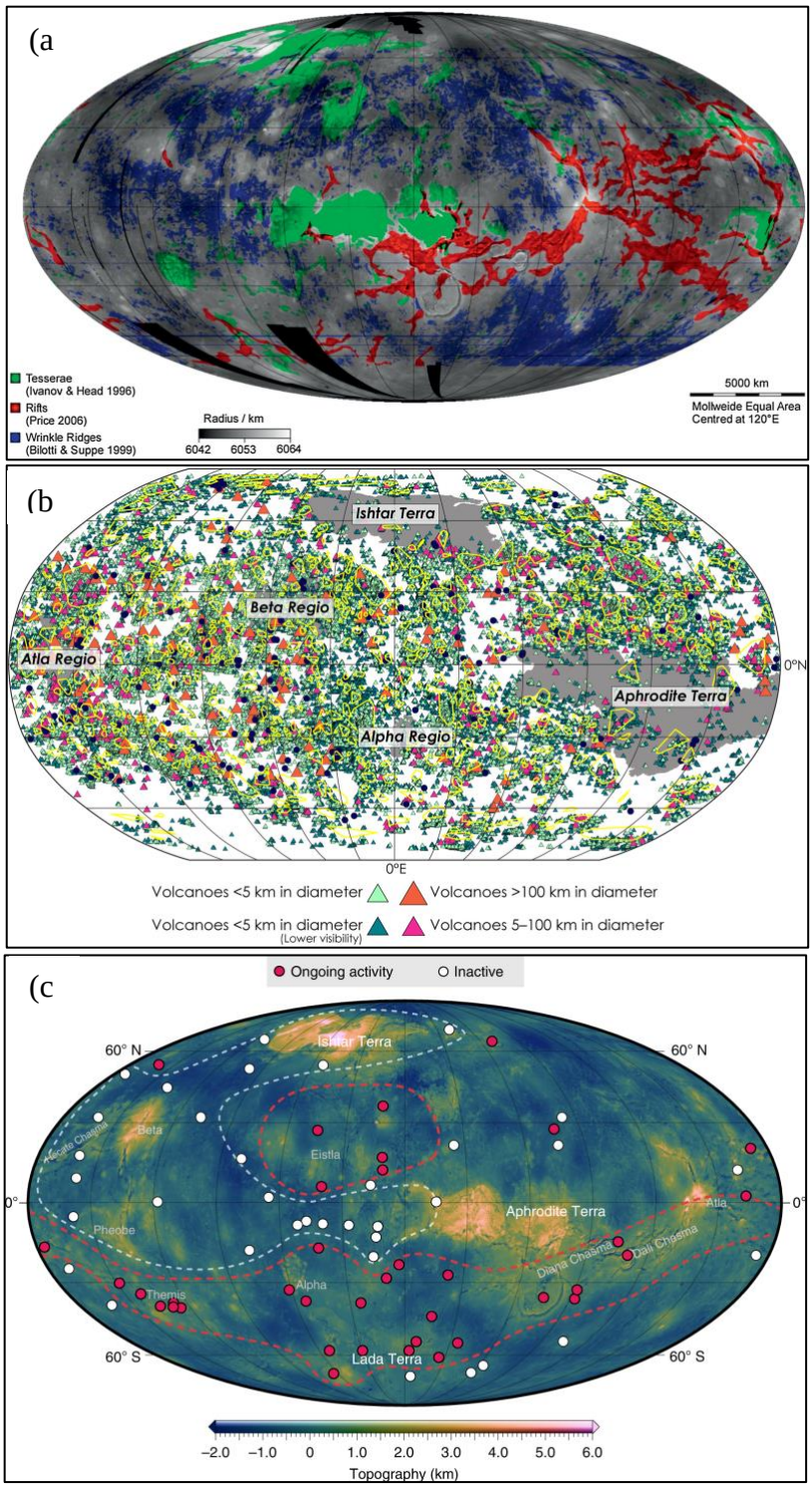

Figure 2. (a) Global map of Venus with tectonic features denoted by color (green: tesserae; red: rifts; blue: wrinkle ridges) from Ghail et al., 2018; (b) Global catalog of volcanoes on Venus, with ~85,000 marked edifices, from Hahn and Byrne, 2023; and (c) Global distribution of hypothesized active (red circles) and inactive (white circles) Venus coronae in relation to mantle upwellings (red dashed lines) from Gülcher et al., 2020.

Idunn Mons (with Olapa Chasma), Ganis Chasma, Maat Mons, and many of the hypothesized active coronae are located in regions inferred to be overlying Venusian hot spots, based on their topography and gravity signatures (McGill et al., 1981; Phillips & Malin, 1984; Stofan et al., 1995), that are either associated with active mantle plumes or passive upwelling due to mantle convection. Therefore, we consider both thermal sources in this work to begin determining which mantle process(es) can produce the magnitude of melt that would sustain these active volcano-tectonic surface features into the present day.

1.4. Motivation for Melt Generation Modeling

While sharing much in common, the differences in both surface and interior conditions on Venus in comparison to Earth indicate that the two bodies have evolved into different geodynamic regimes. The present-day stagnant lid or plutonic-squishy lid regime on Venus changes how much magma is produced and how it is stored in the deep interior as well as how melt is transported to the lithosphere, in comparison to these processes on Earth (**references?**). Investigating magmatic processes will provide context for the existing observations of recent volcanism on Venus as well as implications for volcano-tectonic interactions. To begin characterizing melt production in the deep interior of Venus, I developed a two-dimensional semi-analytical model capable of computing temperature evolution and the associated melt generation in the asthenosphere as function of lithosphere thinning. Using this analytical model, I have quantified melt production rates over time, surface heat flux evolution, and the total area of melt generated in the asthenosphere for 12 parameter sets in order to achieve the following objectives:

1. Determine melt production rate sensitivity to the thermal state of the asthenosphere (under Venusian conditions).

2. Quantify heat transport and loss due to melt generation and lithosphere thinning.
3. Identify modeled parameter sets that could sustain active volcano-tectonic interactions at present.

A primary goal of this work is to use computational models in tandem with past and future mission observations to better constrain Venusian interior conditions and volcanic processes. This is particularly relevant given new observations and measurements of Venus are coming soon with upcoming missions scheduled for the 2030s: NASA's VERITAS and DAVINCI+; and ESA's EnVision. We later discuss how future geophysical investigations during these missions will constrain modeled parameters and our understanding of the Venusian interior as well as how results from this analytical modeling work can assist in interpreting new geophysical datasets (see Section 4.4).

CHAPTER 2.

METHODS

This chapter includes unpublished co-authored material. The methods described in this chapter were developed by me, with input from Dr. Josef Dufek. I independently wrote: 1) the code for the two-dimensional semi-analytical model described below; and 2) this thesis chapter. Dr. Josef Dufek assisted by verifying the derivation of the thermal equations, troubleshooting the analytical model, and providing revision suggestions to this chapter.

A two-dimensional (2D) semi-analytical model was designed and used to constrain the thermal evolution of the Venusian interior due to thinning of the lithosphere, which is assumed to be driven by either convection cells or the presence of a mantle plume in the asthenosphere. This model computes the time-dependent magnitude of lithosphere thinning, temperature, and corresponding melt fraction throughout the 2D model domain for twelve sets of parameters. Parameters include initial surface heat flux, extension rate magnitude, and extension rate decay function with distance from the spreading axis. Pressure-dependent solidus and liquidus temperatures were derived from a nonlinear parameterized batch melting model for anhydrous mantle peridotite (Katz et al., 2003) and used to compute the melt fraction in the asthenosphere. Total melt generated at each time is computed by integrating the melt fraction over the 2D domain of the simulation. We assumed that the newly generated melt was extracted to the lithosphere-asthenosphere boundary (LAB) at each time step, and the model does not consider melt solidification or transport beyond this assumption.

The main outputs from the analytical model are surface heat flux over time and melt production rate. The surface heat flux outputs can be compared to existing estimates of heat flux at Venusian rift systems and/or potential volcanically active regions (e.g., O'Rourke & Smrekar,

2018; Ruiz et al., 2024; Russell and Johnson, 2021) to hypothesize which set of model parameters and which time point(s) in rift evolution best fit the observations. The time-dependent melt production rate informs on the relation between extension rate and melt production and may serve as a proxy for magma flux (i.e., amount of melt intruded into the lithosphere).

2.1. Computational Domain

Model parameters include **(1)** initial surface heat flux (which controls initial lithosphere thickness), **(2)** lithospheric extension (thinning) rate, and **(3)** extension (thinning) rate decay function with distance from the spreading axis. The selected parameter sets are shown in Table 1, which are representative of end-member conditions and hypotheses for present-day Venus.

Table 1. Parameter sets used in the analytical model.

Parameter	**Earth-like heat flux**		**Stagnant lid heat flux**	
	Convection-Driven	**Plume-Driven**	**Convection-Driven**	**Plume-Driven**
Initial surface heat flux (mW/m^2)	-74	-74	-20	-20
Initial crustal thickness (km)	20	20	20	20
Initial lithospheric thickness (km)	26	26	52	52
T_0 (°C)	475	475	475	475
T_{CMB} (°C)	1128.33	1128.33	768.33	768.33
T_{LAB} (°C)	1311.33	1311.33	1312.33	1312.33
Maximum lithosphere thinning rate (mm/yr)	0.1, 1, 10		0.1, 1, 10	
Time step size, dt (years)	10^6, 10^5, 10^4		10^6, 10^5, 10^4	
Model duration (Ma)	260, 26, 2.6		520, 52, 5.2	

The model domain consists of three compositional layers (crust, lithospheric mantle, and upper asthenosphere; Figure 3) with an initial crustal thickness of 20 km in all cases, corresponding to the estimated global average crustal thickness of Venus (Anderson and Smrekar, 2006; James et al., 2013; Jiménez-Díaz et al., 2015). Geochemical data, morphology of volcanic landforms, and crustal thickness estimates imply that the majority of the Venusian crust is basaltic (Grimm and Hess, 1997). The oxide concentrations of surface material at Venus were measured by the Venera and Vega landers, two of which indicated the surface composition is representative of tholeiitic basalt (Treiman, 2007). While not directly sampled or observable, it is hypothesized that the Venusian mantle is similar in composition to a mantle peridotite on Earth with higher MgO content (Trønnes et al., 2019). I assume a tholeiitic basalt composition for the crustal layer and a mantle peridotite composition for the lithospheric mantle and asthenosphere layers in this work. Venera and Vega lander measurements also indicated that the concentration of radiogenic nuclides in the surface material is similar to that on Earth (Treiman, 2007), so I assume a homogenous distribution of radiogenic nuclides throughout the crustal layer, represented by a crustal radiogenic heat term, $H = -8\times10^{-10}$ W/kg. Material properties required for the analytical model (i.e., density, thermal conductivity, etc.) are specific to the composition of each layer (Table 2).

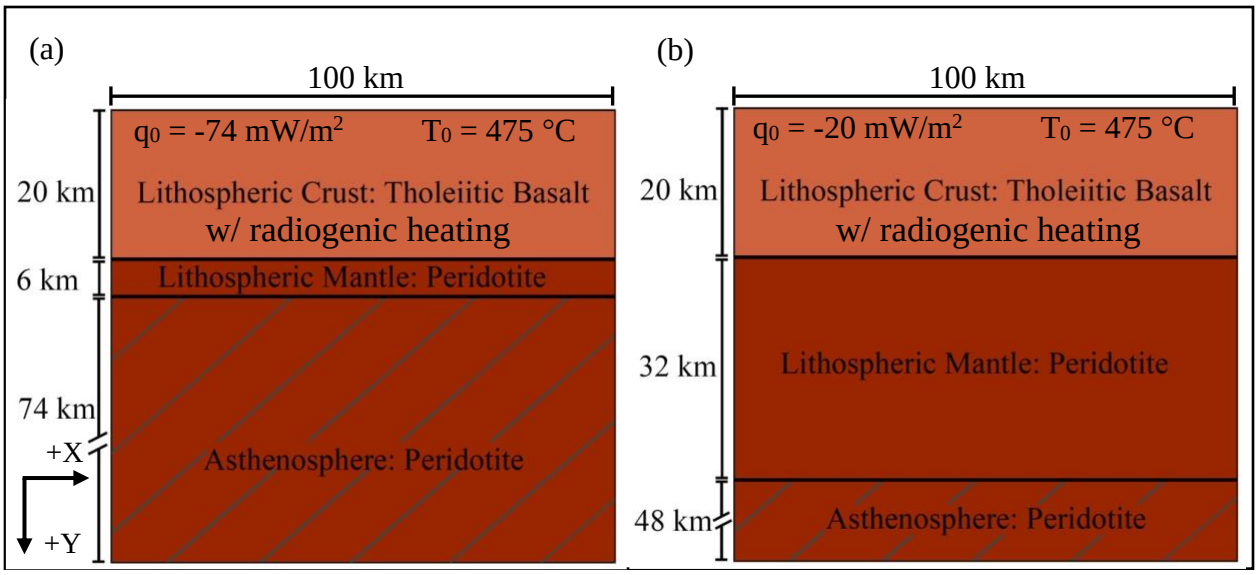

Figure 3. Two-dimensional spatial domain and interior structure for (a) Earth-like initial surface heat flux (q_0 = -74 mW/m^2) and (b) stagnant lid initial surface heat flux (q_0 = -20 mW/m^2). These depictions represent the modeled half-space, where the left boundary of the model domain is the spreading center or plume head center.

Table 2. Material properties of tholeiitic basalt and mantle peridotite.

Material Property	**Variable**	**Value**	**Units**
Thermal conductivity: tholeiitic basalt	κ_{basalt}	3.0	W/m·K
Density: tholeiitic basalt (solid)	ρ_{basalt}	3,000	kg/m^3
Radiative heat term (in crust)	H	-8 × 10^{-10}	W/kg
Thermal conductivity: mantle peridotite*	$\kappa_{peridotite}$	4.0	W/m·K
Density: mantle peridotite (solid)	$\rho_{peridotite}$	3,300	kg/m^3
Thermal expansivity: mantle peridotite**	α_v	4 × 10^{-5}	K^{-1}
Specific heat capacity: mantle peridotite**	c_p	1,260	J/kg·K
$T_{liquidus} - T_{solidus}$: mantle peridotite	ΔT	650	K
Specific latent heat: mantle peridotite	L_s	531 × 10^3	J/kg
Effective specific heat capacity	$c_{p,eff}$	2,077	J/kg·K

*Stacey, 2007; **Computed in MELTS

The spatial domain spans Y = 0-100 km (depth) and X = 0-100 km (distance from spreading axis), with 1 km spacing initially in X and Y for all cases. We chose the maximum depth of 100 km based on the lithospheric thicknesses considered in this work as well as preliminary model outputs that indicated asthenosphere melting is inhibited at greater depths due to high interior pressures. Here, we focus on the convection-driven and plume-driven extension cases, s the spatial extent of the X-domain was determined by assuming the size of a convection cell or radius of a plume head. The flow patterns and size of convective cells depend on many factors, including the material properties and temperature gradient of the mantle, and the dominant interior heat source (basal heating from the core or internal heating from decay of radiogenic nuclides), all of which are poorly constrained for Venus. Although constraints on mantle convection parameters are limited, the size and distribution of surface features, such as rift systems or coronae can be used to infer heat flow patterns in the mantle. The widths of rifts range from <100-400 km (e.g., Gmerek et al., 2024; Guseva and Ivanov, 2019; Magee and Head, 1995) and coronae range in diameter from <100-1,000 km (e.g., Stofan et al., 2001). These wide ranges in size of tectonic features on Venus indicate that convection cells and/or mantle plumes are probably not evenly spaced or consistent in size throughout the interior. Plume head diameters of 100-200 km have been used in mantle plume models for Earth and Venus (e.g., Burov and Cloetingh, 2009; Gülcher et al., 2020). Based on the width of tectonic features on Venus and previously modeled plumes, we assume a 200 km convection cell or plume head diameter in the analytical models (described in Section 2) for convection-driven and plume-driven extension, respectively We assume a system that is symmetric about the spreading axis, so the spatial domain is the half-space of either an upwelling convection cell or plume head.

2.2. Lithosphere Extension Over Time

Extension rates for Venusian rift systems are poorly constrained from available data. Topographic profiles of major rift systems indicate that mantle upwelling and convection could drive sub-crustal extension rates of 20-50 mm/yr (Ghail, 2015), which are comparable to rates for oceanic spreading ridges on Earth, although the crustal extension rate may be much lower. In another study based on terrestrial analogs for Venusian rifts, relationships between topographic profile and spreading rate indicated that Venusian rifts correlate with ultra-slow spreading centers (<12 mm/yr), like the Arctic rift (Stoddard and Jurdy, 2012). The analytical model used in this work is set up to model thinning of the lithosphere rather than directly applying an extensional force at the boundaries. This is a simplification, but the selected thinning rates can be associated with various combinations of extension rate and lithosphere rheology, which is not considered in this work. While thinning rate of the lithosphere is not necessarily equal to extension rate, I used the hypothesized extension rates in Ghail, 2015 and Stoddard and Jurdy, 2012 to inform my choice of thinning rate. Due to high uncertainty in these estimates and my assumptions, I varied the thinning rate parameter at one order of magnitude intervals from 0.1-10 mm/yr, as shown in Table 1.

In this work, we apply a thinning rate to the lithosphere layers of the computational domain (crust and lithospheric mantle) that is dependent on whether the thinning and assumed extension is due to convection in the asthenosphere ("convection-driven") or the presence of a mantle plume near the base of the lithosphere ("plume-driven"; examples of lithosphere thinning for each case are shown in Figure 4). For convection-driven thinning, the thinning rate is constant with depth and decays with distance from the spreading axis, so that the thinning rate is at its maximum at the spreading axis (X = 0) and decays linearly with distance from the spreading

axis, reaching 0 mm/yr at the X = 100 km boundary. For plume-driven thinning, the thinning rate is constant (at the maximum value) across the horizontal radius of the plume, which is equal to the width of the X domain. Because the crust and lithosphere mantle layers are different thicknesses initially, the thinning rates of these layers differ and are computed as shown in Equations 1-2.

$$Thinning\ rate\ (crust) = \frac{initial\ crustal\ thickness}{initial\ lithosphere\ thickness} * Thinning\ rate\ (lith.) \quad (1)$$

$$Thinning\ rate\ (mantle) = \frac{initial\ mantle\ thickness}{initial\ lithosphere\ thickness} * Thinning\ rate\ (lith.) \quad (2)$$

2.3. Derivation of Venusian Thermal Profiles

2.3.1. Initial Thermal Profiles

As the lithosphere thins, the depths to the crust-mantle boundary (CMB) and lithosphere-asthenosphere boundary (LAB) decrease, which increases the thermal gradient. We employ a 1D, steady-state geotherm for the lithosphere, which assumes constant thermal conductivity κ and no internal deformation. This results in the following simplified thermal energy equation for the lithosphere:

$$\kappa \frac{d^2T}{dy^2} + \rho H = 0 \quad (3)$$

where κ is thermal conductivity of rock, T is temperature, y is depth, ρ is density of rock, and H is radiogenic heat (see Table 2 for selected values). Radiogenic heating is only considered in the crust layer, so H = 0 in all cases when computing the lithospheric mantle temperature profile.

We assumed the following initial state boundary conditions to solve Eqn. 3 and determine the depth to the lithosphere-asthenosphere boundary (LAB) for each modeled parameter set: surface heat flux of either q_0 = -20 or -74 mW/m^2, and temperature at the surface, T_0, of 475 °C. The initial surface heat flux is the primary control on the initial lithosphere thickness. Surface heat flux is poorly constrained for Venus, so we consider two end-member values that represent

different geodynamic regimes proposed for present-day Venus: q_0 = -20 mW/m^2 is the low end-member, which represents the stagnant lid regime; and q_0 = -74 mW/m^2 is the high end-member, which represents either an Earth-like heat flux (mobile lid regime) or the plutonic-squishy lid regime. The initial crustal thickness, or depth to the crust-mantle boundary (CMB) y_{CMB} is 20 km and crustal radiogenic heat term is H = -8×10^{-10} W/kg for all parameter sets. These conditions were used to solve Eqn. 3, resulting in

$$T_{crust}(y, t = 0) = T_0 - \left(\frac{q_0}{\kappa_{basalt}} y\right) - \left(\frac{\rho_{basalt} H}{2\kappa_{basalt}} y^2\right) \quad (4)$$

for $0 \leq y \leq y_{CMB}$ = 20 km;

$$T_{mantle}(y, t = 0) = T_{CMB} + \frac{q_{CMB}}{\kappa_{peridotite}} (y_{CMB} - y) \quad (5)$$

for $y > y_{CMB}$ and where q_{CMB} is heat flux at the crust-mantle boundary (Eqn. 6):

$$q_{CMB} = (\rho_{basalt} H y_{CMB}) + q_0 \quad (6)$$

The thermal profiles from Eqn. 4 and 5 were combined to determine the depth to the LAB (y_{LAB}) for each case, which is assumed to correspond to T_{mantle} = 1,300 °C. The integer-value depth point corresponding to the temperature closest to 1,300 °C was selected as y_{LAB}, so T_{LAB} is not exactly 1,300 °C for each parameter set. The initial depth to the LAB is equivalent to the initial lithospheric thickness, which is shown in Table 1 along with the corresponding T_{CMB} and T_{LAB} for each parameter set. The derived lithospheric thicknesses are within estimated ranges derived from gravity and topographic analyses (e.g., Jiménez-Díaz et al., 2015).

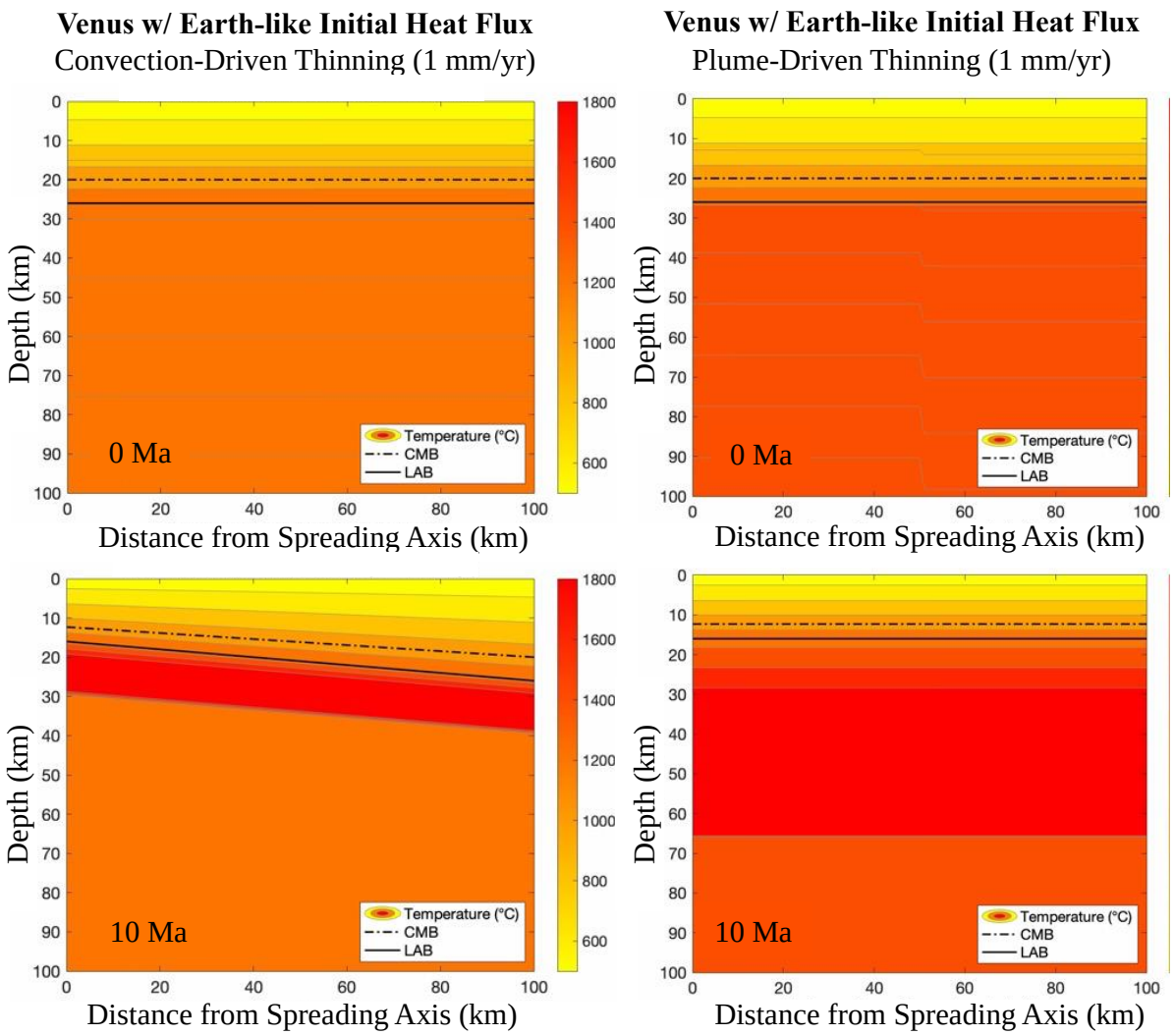

Figure 4. Temperature outputs from analytical model with Earth-like initial heat flux, thinning rate of 1 mm/yr, and (left panels) convection-driven thinning at 0 Ma and 10 Ma; and (right panels) plume-driven thinning at 0 Ma and 10 Ma. The depth of the crust-mantle boundary (CMB) is depicted with a dashed line, the depth to the lithosphere-asthenosphere boundary (LAB) is depicted with a solid black line, and the color bar represents temperature (°C).

2.3.2. Time-Dependent Thermal Profiles

After we determined y_{LAB} for each parameter set, we solved the simplified thermal energy equation (Eqn. 3) with updated boundary conditions: temperature at the surface, T_0, of 475 °C, and temperature at the LAB, T_{LAB}, of ~1,300 °C (T_{LAB} varies slightly for each parameter set, as described in section 2.3.1.). The initial crustal thickness (y_{CMB}) remains 20 km for all parameter

sets, and y_{LAB} is specific to each modeled parameter set (determined by method in section 2.3.1.). Using the updated boundary conditions and computational domains to solve Eqn. 3 gives

$$T_{crust}(\,y(x,t)) = T_0 - \left(y(x,t)\left(\frac{T_0 - T_{CMB}}{y_{CMB}(x,t)} - \frac{\rho_{basalt} H y_{CMB}(x,t)}{2\kappa_{basalt}}\right)\right) - \left(\frac{\rho_{basalt} H}{2\kappa_{basalt}} y(x,t)^2\right) \quad (7)$$

for $0 \leq y \leq y_{CMB}(x,t)$;

$$T_{mantle}(y(x,t)) = T_{LAB} - \left(\frac{(T_{LAB} - T_{CMB})}{(y_{LAB}(x,t) - y_{CMB}(x,t))}\right)(y_{LAB}(x,t) - y(x,t)) \quad (8)$$

for $y_{CMB}(x,t) \leq y \leq y_{LAB}(x,t)$.

The thermal profile of the asthenosphere differs for the convection-driven and plume-driven thinning assumptions. For the convection-driven case, temperature in the asthenosphere was computed from $y_{LAB}(x,t)$ up to 100 km depth. Here we assumed an adiabatic, isentropic asthenosphere with no conductive heat loss:

$$\frac{dT}{dy} = \frac{\alpha_v g T}{c_p} \quad (9)$$

where α_v is thermal expansivity of mantle peridotite, g is gravitational acceleration (8.87 m/s^2), and c_p is specific heat capacity of mantle peridotite (see Table 2 for selected values). When solved for the time-dependent boundary conditions, Eqn. 9 gives

$$T_{asthenosphere}(y(x,t)) = T_{LAB} e^{\alpha_v g (y(x,t) - y_{LAB}(x,t))/c_{p,eff}} \quad (10)$$

for $y > y_{LAB}(x,t)$;

$$c_{p,eff} = c_p + \left(\frac{L_s}{\Delta T}\right) \quad (11)$$

where $c_{p,eff}$ is effective specific heat capacity (Eqn. 11), which includes thermal effects due to phase change, L_s is specific latent heat, and ΔT is the difference between the liquidus and solidus temperatures (of mantle peridotite here). Although melt is not present at all spatial and/or time points in the asthenosphere layer, we used $c_{p,eff}$ for all $T_{asthenosphere}$ calculations to simplify

the analytical model. This choice results in slightly underestimating the temperature throughout the asthenosphere at space/time points where melt is not present, but we prefer this over overestimating $T_{asthenosphere}$ and the corresponding melt fraction outputs.

For the plume-driven thinning case, we assume that the asthenosphere layer is filled by a mantle plume head. Plume excess temperatures in Earth's upper mantle are 250-350 °C (e.g., Farnetani, 1997; Schilling, 1991; Zhong, 2006), so we apply a maximum plume temperature of 1,550 °C over a 50 km radius in the X-direction, starting at 10 km below the LAB, and then an elevated temperature of 1,425 °C at all other points in the asthenosphere, which represents the outer layer of the plume (Figure 4).

The (X, Y) grid in the analytical model is updated based on the decreasing $y_{CMB}(x,t)$ and $y_{LAB}(x,t)$ depth values at every time step. T_{CMB} and T_{LAB} are constant for all time points because they are prescribed boundary conditions. Temperature is computed for every (X, Y) grid point at evenly distributed time steps (*dt*) until the magnitude of total thinning equals the original lithospheric thickness (Figure 4). The time step sizes are dt = 10^6, 10^5, and 10^4 years for the 0.1, 1, and 10 mm/yr thinning rates, respectively, and total model duration is dependent on the initial lithosphere thickness and thinning rate (shown in Table 1).

2.4. Asthenosphere Melt Fraction Calculation

Using the Katz et al., 2003 anhydrous mantle peridotite parameterization, I computed pressure-dependent solidus and liquidus temperatures for a mantle peridotite under Venusian pressure conditions (Eqns. 12-13).

$$T_{solidus} = 1085.7\,℃ + \left(132.9\ \frac{℃}{\mathrm{GPa}}\right) P_{asth}(x,y,t) + \left(-5.1\ \frac{℃}{GPa^2}\right) P_{asth}(x,y,t)^2 \quad (12)$$

$$T_{liquidus} = 1780.0\,℃ + \left(45.0\ \frac{℃}{\mathrm{GPa}}\right) P_{asth}(x,y,t) + \left(-2.0\ \frac{℃}{GPa^2}\right) P_{asth}(x,y,t)^2 \quad (13)$$

where P_{asth} is pressure (in GPa) in the asthenosphere layer (assuming surface pressure is 9.20 MPa). Then melt fraction in the asthenosphere was computed from the time- and depth-dependent $T_{asthenosphere}$, $T_{solidus}$, and $T_{liquidus}$ as

$$Melt\ Fraction(x,y,t) = \frac{T_{asthenosphere}(x,y,t) - T_{solidus}(x,y,t)}{T_{liquidus}(x,y,t) - T_{solidus}(x,y,t)} \quad (14)$$

Melt fraction between the solidus and liquidus is assumed to be a linear function of temperature. The solidus temperature, liquidus temperature, and melt fraction were computed at each (X, Y) grid point in the computational domain at every time step. Regions in the asthenosphere that melted at an earlier time step are not allowed to remelt if the melt fraction exceeded 0.05. The choice of melt fraction > 0.05 is arbitrary but informed by the expected compositional changes of a melting mantle peridotite – i.e., after a solid peridotite has produced 5% melt, its composition has been altered such that the melt parameterization for a mantle peridotite is no longer applicable. We do not track geochemical evolution of the melt or solid rock in this analytical model, so we conservatively limit remelting throughout the asthenosphere layer.

2.5. Melt area and Extracted Melt Layer Thickness Calculations

The magnitude of melting was quantified as a 2D melt area. To compute melt area, the analytical model defines the melt fraction isolines at 0.01 resolution for melt fraction = 0.00 – 0.50. The melt fraction isolines were used to map the distribution of melt and to compute newly generated melt area in the asthenosphere layer at each time point. After defining the isolines, the model uses numerical integration via the trapezoidal method to compute the area under each isoline curve, and the difference between consecutive isolines is the melt area corresponding to a specific melt fraction. In this work, we always round melt fraction down so that we underestimate the total melt area rather than overestimate. For example, the area between the 0.01 and 0.02 melt fraction isolines will be considered as a region with 0.01 melt fraction. The

total melt area represents the newly generated melt at each time step, and is computed by the following sum:

$$Total\ Melt\ Area\ (t) = 2 * \sum_{i=0}^{0.49} melt\ fraction_i * (integrated\ area_{i+0.01} - \ integrated\ area_i) \quad (15)$$

where the integrated area is the area under each isoline curve, computed by numerical integration. The sum is multiplied by two since the model runs computations over a symmetric half-space.

The new melt generated at each time step is instantaneously extracted to the base of the LAB and is evenly distributed in the X-direction across the model domain width (100 km). This extracted melt layer is assumed to have a melt fraction of 1.00 and temperature equal to the liquidus. The extracted melt layer thickness is equal to the melt area at time *t* divided by the width of the model domain (100 km in this work), which is added to all previously extracted melt. This extracted melt layer thickness is updated at every time step, and the (X, Y) grid is also updated at every time step to include the growing melt layer. We do not consider additional melting that may be driven by the elevated temperature of the extracted melt layer or transport of extracted melt into the lithosphere in this work. Additionally, the assumption that temperature of the melt layer is equal to the liquidus temperature of mantle peridotite has no effect on the $T_{asthenosphere}$ calculations.

2.5.1. Instantaneous Melt Extraction Assumption

A simple calculation to compute melt ascent velocities using Darcy's law for static porous media flow indicated that melt would rise to the LAB on timescales on the order of 10^3-10^4 years (depending on depth of melting and melt fraction), while the time steps considered in this work are $\geq 10^4$ years. Because all melt in the model domain would reach the LAB within the duration of each timestep, it is justified to assume "instantaneous" extraction to the LAB. Additionally,

other proposed modes of melt extraction operate at rates faster than static porous media flow (e.g. reactive transport, compaction, etc). However, greater extension rates would decrease the time step duration, so melt migration and vertical ascent should be tracked if larger extension rates are considered in future work.

2.6. Melt Production Rate Calculation

We estimate a melt production rate from the melt area generated at each time step, which may be a proxy for magma flux (i.e., the amount of melt intruded into the lithosphere). Melt production rate is computed as

$$Melt\ Production\ Rate\ (t) = \frac{Total\ Melt\ Area\ (t)}{2 * X_{max} * dt} \tag{16}$$

where X_{max} is the width of the computational domain (100 km) and *dt* is the time step size.

2.7. Surface Heat Flux Calculation

Surface heat flux q_0 changes due to thinning of the lithosphere over time. Here, we calculate surface heat flux over time as

$$q_0(x, y = 0, t) = -\kappa \frac{dT_{crust}}{dy} = -\kappa_{basalt} \left[\frac{-(T_0 - T_{CMB})}{y_{CMB}} + \left(\frac{\rho_{basalt} H y_{CMB}}{2\kappa_{basalt}} \right) \right] \tag{17}$$

where dT_{crust} refers to the time-dependent thermal profile of the crustal layer (Eqn. 7).

CHAPTER 3.

RESULTS

This chapter includes unpublished co-authored material. The results described in this chapter were generated by analytical model simulations that I set up and ran. I made all the figures and tables presented here, and I independently wrote this thesis chapter. Dr. Josef Dufek assisted by providing revision suggestions to this chapter.

The key outputs from the analytical model are melt area, melt production rate, extracted melt layer thickness, and surface heat flux, all of which change over time. The parameter sets considered in this work are grouped by the selected combinations of initial heat flux and thinning mechanism, and each parameter set was modeled for three extension rates (Table 1). Within a given parameter set (e.g., Earth-like heat flux, convection-driven thinning), the total amount of melt generated from the model is the same for each extension rate, and the trends of melt area and extracted melt layer thickness are identical when considering the ratio of lithosphere thinning magnitude to initial lithospheric thickness instead of time (model duration varies considerably for each parameter set due to varying the thinning rate by orders of magnitude). These results are the same magnitude because each model runs until the magnitude of thinning equals the initial lithosphere thickness.

Surface heat flux (Figure 5) increases exponentially as the lithosphere thins for all modeled parameter sets. For a given initial heat flux (e.g., q_0 = -20 or -74 mW/m^2), the surface heat flux over time was the same for convection- and plume-driven thinning and all considered extension rates.

3.1. Parameter Set: Earth-Like Initial Heat Flux, Convection-Driven Thinning

3.1.1. Melt Area and Melt Production Rate

For the modeled parameter set with an Earth-like initial heat flux (-74 mW/m^2) and convection-driven thinning, a total of ~8,430 km^2 of melt was produced (this result is the same for each extension rate; Table 3). The amount of newly generated melt at each time point, and therefore the melt production rate, vary over the model run time (Figures 6-7). During the first ~14% of the model duration, 10-100s of km^2 of melt are produced at each time point. After a large decline in melt production, this parameter set produces ~1-9 km^2 of melt for the remainder of the model run. This parameter set reaches a quasi-steady state around 40% run time with an average melt area of ~5.9 km^2 at each time point, but the melt area decreases slowly from this time point to the end of the model run.

Melt production rate is computed from the melt area generated at each time point, so this result follows the same trend as the newly generated melt area results (see Figures 6-7). However, melt production rate is also dependent on time and therefore the thinning rate. For the first ~14% of the model duration, melt production rates are at their highest and range from: ~0.1 – 3.6 mm/yr for dTh/dt = 0.1 mm/yr; ~1 – 36 mm/yr for dTh/dt = 1 mm/yr; and ~10 – 360 mm/yr for dTh/dt = 10 mm/yr. For the rest of the model duration, melt production rate reaches a near constant value of 0.03, 0.3, 3 mm/yr for dTh/dt = 0.1, 1, and 10 mm/yr, respectively (Figure 7; Table 3).

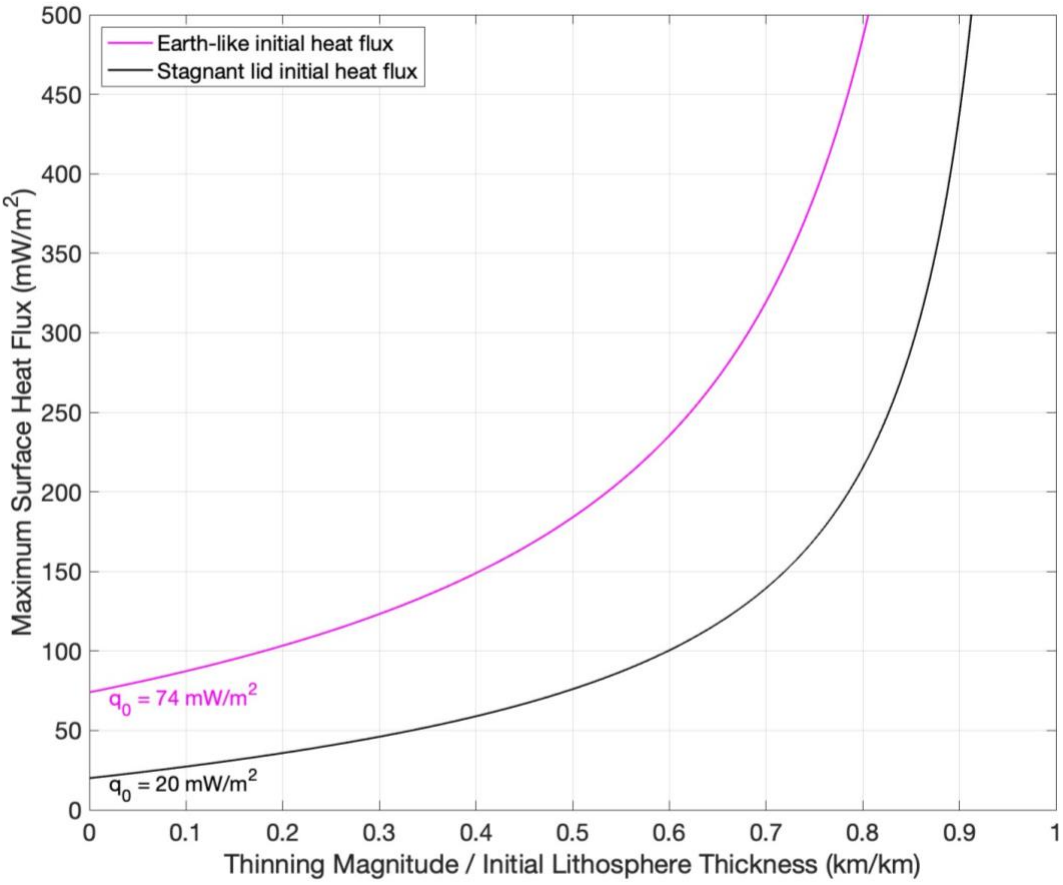

Figure 5. Absolute value of the maximum surface heat flux (at X = 0) versus the ratio of thinning magnitude at time *t* to initial lithosphere thickness for the Earth-like (magenta) and stagnant lid (black) initial heat flux parameter sets. The maximum surface heat flux over time was the same, for a given initial heat flux, for the convection- and plume-driven thinning cases and all considered extension rates. The x-axis is a non-dimensionalized proxy for time since model duration depends on initial lithosphere thickness and extension rate, which are varied across parameter sets.

3.1.2. Extracted Melt Layer Thickness

Most of the melt (~85%) was produced in the first 14% of the model run time, so that the extracted melt layer was 35.8 km thick. After this time point, the melt layer thickness increases steadily, following a near linear trend with a shallow slope of <1 km per 0.10 thinning magnitude/initial lithosphere thickness ratio. The final thickness of the extracted melt layer was 42.2 km (Figure 8; Table 3).

Table 3. Summary of analytical model results for total generated melt, equilibrium melt production rate, extracted melt layer thickness, and estimated lithosphere growth.

Result		Earth-like heat flux		Stagnant lid heat flux	
		Convection-Driven	**Plume-Driven**	**Convection-Driven**	**Plume-Driven**
Total Generated Melt (km^2)		8,430	9,920	11,900	8,060
Equilibrium Melt Production Rate (mm/yr)	**dTh/dt (mm/yr)**				
	0.1	0.03	0	0.1	0
	1	0.3	0	1	0
	10	3	0	10	0
Final Melt Layer Thickness (km)		42.2	49.6	59.4	40.3
Initial Lithosphere Thickness (km)		26	26	52	52
Percent Lithosphere Growth		62%	91%	14%	–23%

3.2. Parameter Set: Earth-Like Initial Heat Flux, Plume-Driven Thinning

3.2.1. Melt Area and Melt Production Rate

For the modeled parameter set with an Earth-like initial heat flux (-74 mW/m^2) and plume-driven thinning, a total of 9,920 km^2 of melt was produced (this result is the same for each extension rate; Table 3). In this case, the amount of newly generated melt at each time point decreases rapidly to zero within the first 10% of model run time (Figure 6). The maximum amount of melt (9,860 km^2) is generated at the first time point, and then melt production drops to ~10 km^2 at the next time point. New melt area decreases from ~10 to <1 km^2 by ~6% of the model run time, following a step-function trend where melt area is constant for short periods and then decreases.

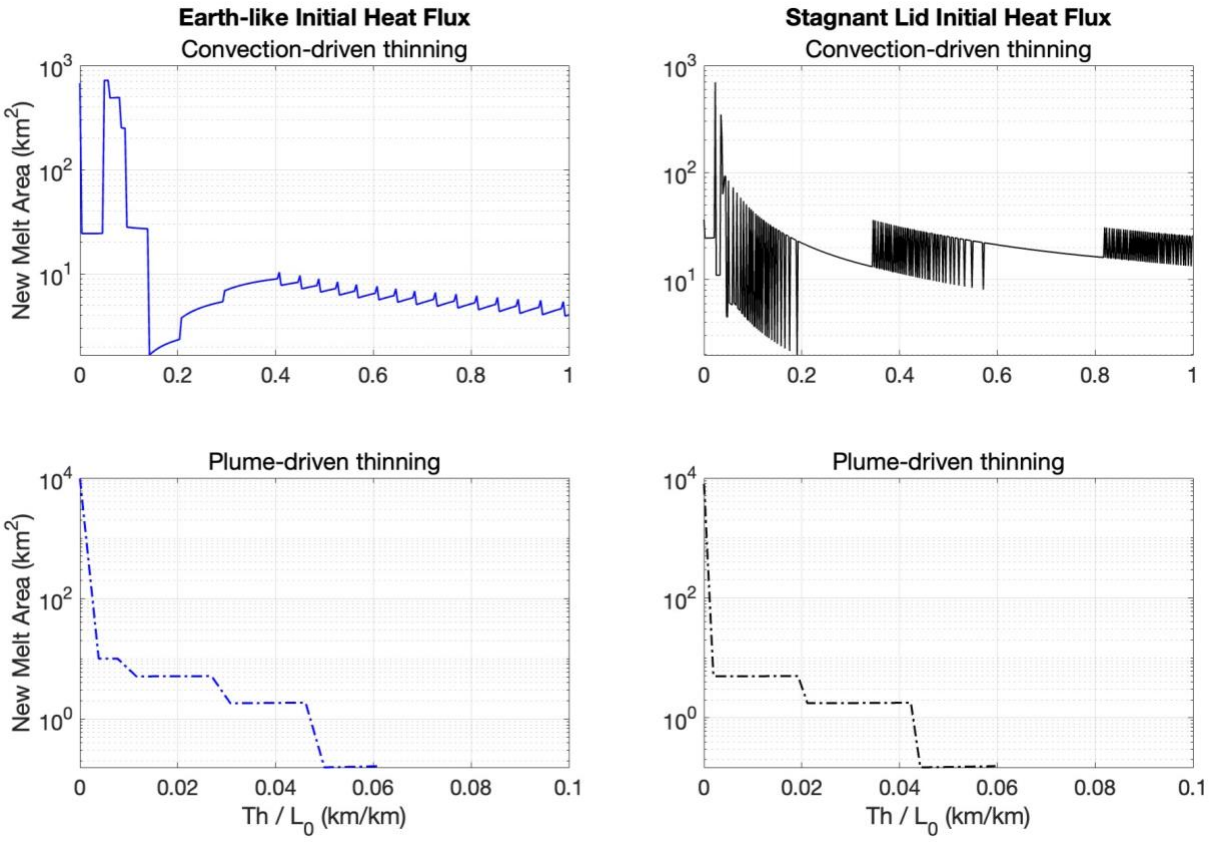

Figure 6. New melt area generated at each time step versus the ratio of thinning magnitude at time *t* (Th) to initial lithosphere thickness (L_0) for each modeled parameter set. The x-axis is a non-dimensionalized proxy for time since model duration depends on initial lithosphere thickness and extension rate, which are varied across parameter sets.

As mentioned before, melt production rate follows the same trend as the newly generated melt area results (see Figures 6-7), but varies with thinning rate. The maximum melt production rate at the first time point is ~49 mm/yr yr for dTh/dt = 0.1 mm/yr; ~490 mm/yr for dTh/dt = 1 mm/yr; and ~4,900 mm/yr for dTh/dt = 10 mm/yr. After the first time step, the melt production rate decays rapidly down to 0.05 mm/yr, 0.5 mm/yr, and 5 mm/yr for dTh/dt = 0.1 mm/yr, 1 mm/yr, and 10 mm/yr, respectively. Following the decreasing step function trend, melt production rate decreases to zero by ~6% of the model run time, so this parameter set does not reach an equilibrium state.

3.2.2. Extracted Melt Layer Thickness

All melt was produced in the first 6% of the model run time for the Earth-like heat flux, plume-driven thinning parameter set. The extracted melt layer thickness is 49.3 km at the first time point and rapidly increases to a total melt layer thickness of 49.6 km (Figure 8; Table 3).

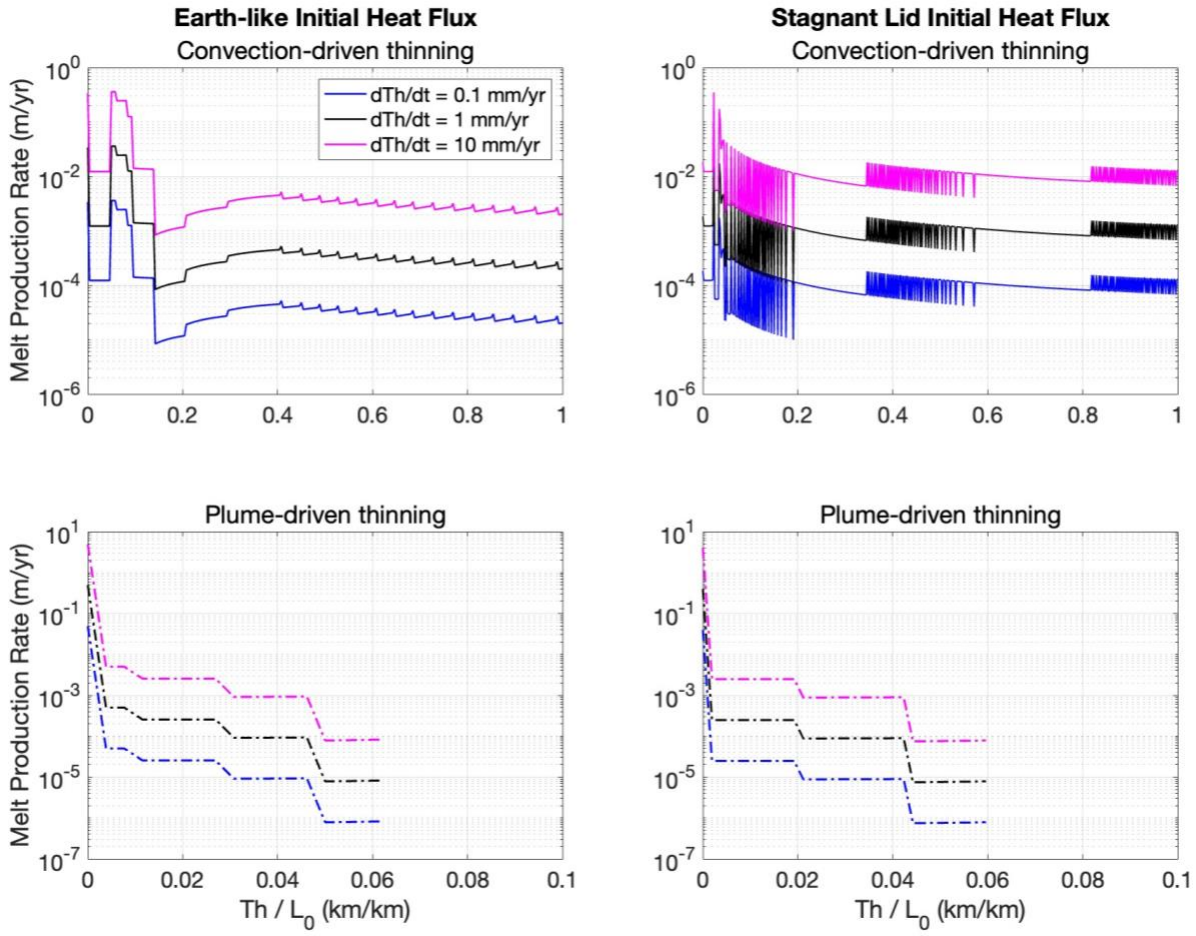

Figure 7. Melt production rate versus the ratio of thinning magnitude at time *t* (Th) to initial lithosphere thickness (L_0) for each modeled parameter set. The three considered thinning rates (dTh/dt) are plotted for each parameter set, where blue represents dTh/dt = 0.1 mm/yr, black represents dTh/dt = 1 mm/yr, and magenta represents dTh/dt = 10 mm/yr. The x-axis is a non-dimensionalized proxy for time since model duration depends on initial lithosphere thickness and extension rate, which are varied across parameter sets.

3.3. Parameter Set: Stagnant Lid Initial Heat Flux, Convection-Driven Thinning

3.3.1. Melt Area and Melt Production Rate

For the modeled parameter set with a stagnant lid initial heat flux (-20 mW/m^2) and convection-driven thinning, a total of 11,900 km^2 of melt was produced (this result is the same for each extension rate; Table 3). This is the largest total melt area of the modeled parameter sets. Similar to the previously described parameter sets, the maximum melt generated in one time step (~700 km^2) occurs at the beginning of the model run. However, the new melt area and melt production rate for the stagnant lid heat flux with convection-driven thinning parameter set follow a unique trend over time in comparison to the other modeled parameter sets (Figures 6-7). Over the full model duration, we see three separated time periods of large periodic variations in melt productivity, with new melt area varying from <10 km^2 to 10s of km^2 generated at alternating time points. These high frequency, periodic trends are separated by periods of near constant decrease in melt generation. The range of melt area in the periodic regions (i.e., amplitude) decreases over time, and new melt area is consistently between ~10-30 km^2 (19.8 km^2 average) after ~20% of the model run time, indicating that this parameter set reaches a quasi-equilibrium state.

Melt production rates range from 0.01 – 3.5 mm/yr for dTh/dt = 0.1 mm/yr; 0.1 – 35 mm/yr for dTh/dt = 1 mm/yr; and 1 – 350 mm/yr for dTh/dt = 10 mm/yr, with the maximum occurring within the first 5% of the model duration. As described above this parameter set reaches a quasi-equilibrium state at ~20% of the model run time, and the average melt production rates are equal to the corresponding thinning rates: 0.1, 1, and 10 mm/yr for dTh/dt = 0.1 mm/yr, 1 mm/yr, and 10 mm/yr, respectively (Figure 7; Table 3).

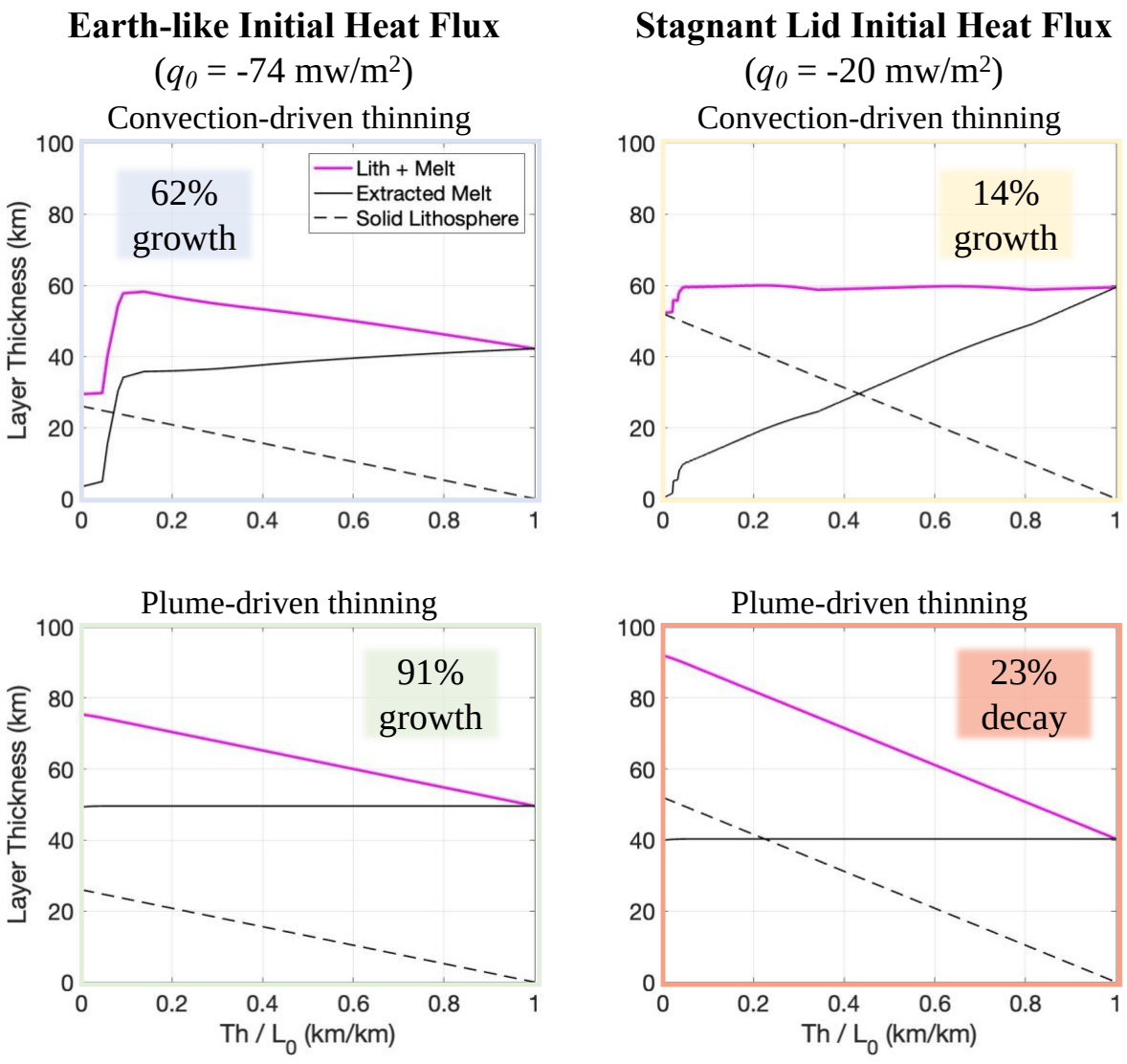

Figure 8. Lithosphere thickness (dashed black line), extracted melt layer thickness (solid black line), and the sum of lithosphere and extracted melt thicknesses (solid majenta line) versus the ratio of thinning magnitude at time *t* to initial lithosphere thickness for each modeled parameter set. The x-axis is a non-dimensionalized proxy for time since model duration depends on initial lithosphere thickness and extension rate, which are varied across parameter sets.

3.3.2. Extracted Melt Layer Thickness

At 5% of the model run time (when maximum melt production occurs), the extracted melt layer thickness is 10.2 km. After this initial period of maximum melt production, the extracted

melt layer thickness increases about linearly with a slope of ~5 km per 10% model duration, and the final thickness of the extracted melt layer was 59.4 km (Figure 8; Table 3).

3.4. Parameter Set: Stagnant Lid Initial Heat Flux, Plume-Driven Thinning

3.4.1. Melt Area and Melt Production Rate

For the modeled parameter set with a stagnant lid initial heat flux (-20 mW/m^2) and plume-driven thinning, a total of 8,060 km^2 of melt was produced (this result is the same for each extension rate; Table 3). The melt area and melt production rate for this parameter set are nearly identical in magnitude in trend to those for Earth-like initial heat flux and plume-driven thinning parameter set (Figures 6-7). For this parameter set, generated melt area decreases from ~8,000 to ~5 km^2 in one time step and then follows a decreasing step function trend until generated melt area reaches 0 km^2 at 6% of the model run time. Similarly, melt production rate maxima are 40 mm/yr, 400 mm/yr, and 4,000 mm/yr for dTh/dt = 0.1 mm/yr, 1 mm/yr, and 10 mm/yr, respectively at the first time point, and then melt production rates decrease to zero via a step function trend (Figure 7). An equilibrium state is not reached for this parameter set.

3.4.2. Extracted Melt Layer Thickness

Like the Earth-like heat flux, plume-driven thinning parameter set, all melt was produced in the first 6% of the model run time for the stagnant lid heat flux, plume-driven thinning parameter set. The extracted melt layer thickness is ~40.0 km at the first time point and rapidly increases to a total melt layer thickness of 40.3 km (Figure 8), which makes this the only parameter set to have a final melt layer thickness that is less than the initial lithosphere thickness (Table 3).

CHAPTER 4

DISCUSSION

This chapter includes unpublished co-authored material. I devised the interpretations and discussions of the results described in this chapter and independently wrote this thesis chapter. Dr. Josef Dufek assisted by suggesting additional discussion topics to consider and providing revision suggestions to this chapter.

4.1. Interpretation and Comparison of Results

The parameter sets that assumed convection-driven thinning in this work show potential for achieving an equilibrium state, where melt production rate is near constant or fluctuates over a narrow range. Because the temperature profile in the asthenosphere is adiabatic in the convection case, melting is limited to between the LAB and ~65 km depth, beyond which asthenosphere temperatures do not exceed the solidus of mantle peridotite. As the lithosphere thins over time, new (previously unmelted) regions of the asthenosphere rise to depths where melting can occur, which sustains an extensional melting system over long durations, based on the model results for the Earth-like and stagnant lid initial heat flux with convection-driven thinning parameter sets. The quasi-equilibrium state melt production rates and the final thicknesses of the extracted melt layer in comparison to the initial lithosphere thicknesses are shown in Table 3. In all cases, we can assume that the extracted melt eventually adds to the lithosphere thickness, regardless of whether the melt solidifies at the LAB, in the lithosphere, or at the surface post-eruption.

For the parameter set with Earth-like initial heat flux and convection-driven thinning, the equilibrium melt production rates are about one order of magnitude less than the corresponding thinning rates (dTh/dt), indicating that melt production would not keep up with lithosphere thinning once equilibrium is reached. However, melt production rates are 1-2 orders of

magnitude higher at the beginning of the model run than those during the equilibrium state for this parameter set (all thinning rates), so substantial melt is produced early on to sustain the lithosphere. The melt layer thickness results indicate that the lithosphere thickness would increase by 62% (~16 km) for this parameter set when all generated melt solidifies.

For the stagnant lid, convection-driven parameter set, the equilibrium melt production rates are roughly equivalent to the corresponding thinning rates, which suggest that the initial lithospheric thickness is maintained over time. Because of this and the elevated melt production rates at the start of the model runs, the lithosphere is expected to increase in thickness by 14% (~7 km) based on the final extracted melt layer thickness. The lithosphere does not grow as much for this parameter set in comparison to the earth-like heat flux, convection-driven thinning case for two reasons: 1) the stagnant lid case reaches equilibrium at ~20% of the model duration, which is half the time it takes for the earth-like heat flux, convection-driven thinning case to reach equilibrium, and 2) deviations from the equilibrium melt production rate early in the model run are not as large for the stagnant lid case.

In contrast, the plume-driven thinning cases produced a large batch of melt initially due to the elevated asthenosphere temperatures that were selected to represent the presence of an upper mantle plume. After this initial batch of melting, small amounts of melting (<0.05 melt fraction) occur in the outer region of the mantle plume, where the temperature is 1,425 °C, over the full duration of the model run; this temperature is less than the solidus at depths greater than ~98 km. All melting happens within the first ~6% of model run time for both plume-driven thinning parameter sets, so these cases do not reach an equilibrium melt production state. This result suggests that plume-driven systems will be very short-lived and unsustainable over longer durations. However, mantle plumes may be rejuvenated over time, transporting more melt to

shallow depths, as the plume tail continues to rise, which is not modeled in this work. Additionally, the conservative rule that partially melted regions of the asthenosphere cannot continue melting at later times within the analytical model is particularly limiting for the plume-driven parameter sets. The elevated asthenosphere temperatures (up to 1,550 °C) would likely exceed the solidus of the altered (due to partial melting) mantle compositions, although the geochemical evolution due to partial melting is not tracked in this work. The lithospheric thickness increased by 91% for the Earth-like initial heat flux, plume-driven thinning parameter set and decreased by 23% for the stagnant lid initial heat flux parameter set. Because the total generated melt areas are about the same for both plume-driven parameter sets, the differences in lithosphere growth/decay are attributed to the difference in initial lithosphere thickness for the earth-like and stagnant lid heat flux; the initial lithosphere thickness for the stagnant lid heat flux is double that for the Earth-like heat flux, so more melting is required to sustain the stagnant lid lithosphere. More detailed treatment of mantle plume dynamics and melt geochemistry is required to adequately assess plume-driven thinning and melting.

4.2. Melt Evolution and Transport Beyond Analytical Model Capabilities

The analytical model presented in this work only computes melting in the asthenosphere, so the results do not provide any detail on what happens to the generated melt after extraction to the LAB. Two possible paths of melt evolution are 1) diking occurs due to melt layer buoyancy forces exceeding the strength of the lithosphere and transports melt to some depth in the lithosphere, either forming a shallow magma reservoir or erupting at the surface depending on dike length and lithosphere thickness; or 2) the extracted melt does not generate buoyancy forces large enough to fracture the overlying lithosphere, so it remains at the LAB cooling and solidifying (at least partially) over time, depending on thermal conditions. In future work, the

fate of the extracted melt layer could be determined by following methods from Bland and Elder, 2022; Havlin et al., 2013; and references therein to compute dike formation and melt transport at the LAB.

While we do not compute the magnitude of melt transport into the lithosphere here, the melt production rates computed in this work can be used as a proxy for magma flux or magma emplacement rates (i.e., how much melt intrudes into the lithosphere). Magma fluxes specific to oceanic hot spots, continental hot spots, and oceanic ridges on Earth were estimated from the magma emplacement rates for these settings in Crisp, 1984 and compared to the modeled melt production rates. Magma flux was estimated as 10^{-2} – 10^{-1} m/yr for oceanic spreading ridges and 10^{-3}–10^{-2} m/yr for hot spot settings on Earth. The modeled equilibrium melt production rates for the Earth-like initial heat flux, convection-driven thinning case (10^{-5}, 10^{-4}, and 10^{-3} m/yr for the 0.1, 1, and 10 mm/yr thinning rates, respectively) are low in comparison to terrestrial magma fluxes at convection-driven extensional settings (e.g., oceanic spreading ridges), but they are comparable to magma fluxes at terrestrial hot spot settings. While we do not interpret the melt production rates for both plume-driven parameter sets as reaching an equilibrium state, the average values after the initial batch of melting (<1% model duration) are the same order of magnitude as the melt production rates for the Earth-like initial heat flux, convection-driven thinning parameter set, and so these plume-driven thinning results are comparable to magma fluxes at terrestrial hot spot settings despite being short-lived. The modeled melt production rates for the stagnant lid initial heat flux, convection-driven case (10^{-4}, 10^{-3}, and 10^{-2} m/yr for the 0.1, 1, and 10 mm/yr thinning rates, respectively) are also most similar to the terrestrial hot spot settings, although the melt production rate of 10^{-2} m/yr for the 10 mm/yr thinning rate is also comparable to the terrestrial values for oceanic spreading ridges. It is important to point out that

not all of the melt generated in the asthenosphere will always intrude into the lithosphere, so it is likely that melt production rates are typically greater than magma fluxes on any planetary body. Overall, these comparisons suggest that the Venusian interior undergoes less melting than Earth's interior at what are inferred to be similar tectonic/volcanic settings. Lastly, the magmatic volume production rate (29 km^3/yr) and global length of rifts (55,000 km) on Venus provided in Ghail, 2015 were used to estimate magma flux (~10^{-1} m/yr) at Venusian rifts, which is an order of magnitude higher than the largest equilibrium state production rate computed in this work.

4.3. Implications for Present-Day Volcanic Activity on Venus

In addition to relating melt production rate to magma flux, hypothesized intrusive-to-extrusive ratios or "magmatic eruption efficiency" (Figure 9) can inform estimates for magnitudes of intruded or erupted melt. On Earth, it has been estimated that only 10-20% of generated melt is erupted (extrusive) on average, but this value is strongly dependent on factors such as tectonic setting and regional interior structure and composition (Cawood et al., 2012; Crisp, 1984). Figure 9 provides values of magmatic eruption efficiency (i.e., the percent of magma that is erupted) as a function of lithosphere strength (yield stress) and geodynamic regime (figure from Rolf et al., 2022). The two regimes debated for Venus at present differ greatly in expected magmatic eruption efficiency, where 0-30% of generated melt is estimated to erupt for the plutonic-squishy lid and 30-90% of generated melt is estimated to erupt for the stagnant lid regime. Future geophysical measurements that constrain the interior and detections of active eruptions (or a lack thereof) during upcoming missions at Venus (described further in Section 4.4) will provide more insight on the present-day intrusive-to-extrusive ratios and magmatic eruption efficiency. Prior to these missions, the work presented here could be expanded to use end-member magmatic eruption efficiencies to estimate eruptive area (or

volume for an assumed rift segment length) over time from the generated melt area results. Then these eruptive area estimates can be compared to sizes of volcanic edifices and lava flows on the surface that have been suggested to be geologically young. This comparative analysis would indicate which modeled cases produce enough melt to form the observed surface features.

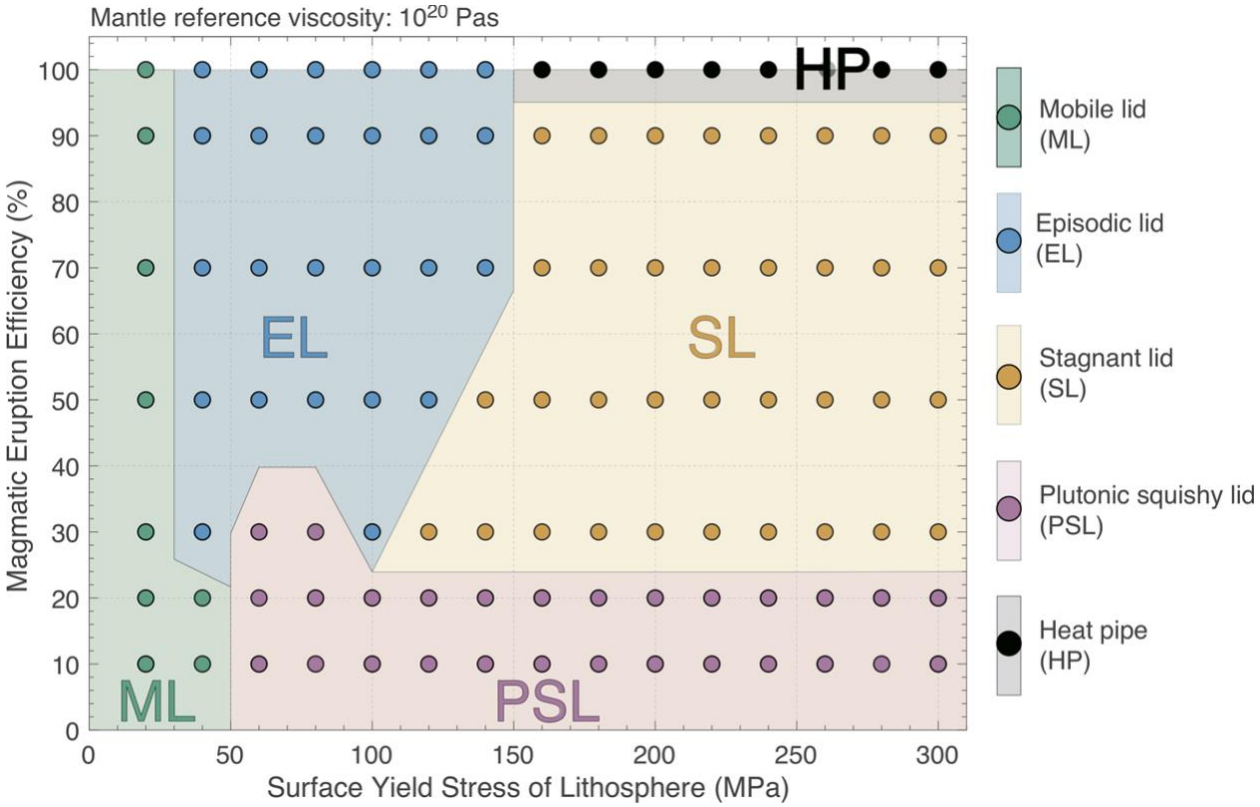

Figure 9. Magmatic eruption efficiency (i.e., percent of magma that is erupted) as a function of lithosphere yield stress (strength) and geodynamic regime. Each geodynamic regime is described in Section 1.1, aside from the heat pipe regime, which is not hypothesized for present-day Venus. The stagnant lid and plutonic-squishy lid regimes are most relevant to this work. Figure from Rolf et al., 2022.

4.4. Connection to Future Mission Measurements

The upcoming NASA and ESA missions, VERITAS and EnVision, respectively, will conduct geophysical investigations and search for active volcanism on Venus. The VERITAS mission will have an X-band interferometric synthetic aperture radar (InSAR), an infrared

spectrometer, and a gravity science investigation, and the EnVision mission will include an S-band synthetic aperture radar (SAR) with radiometry and altimetry capabilities, a spectrometer with infrared and ultraviolet channels, a subsurface radar sounder, and a gravity science investigation. For the deep interior, the gravity science investigations will provide new constraints on the state of the core, core size, and viscous response of the interior by measuring the moment of inertia factor, tidal Love number, and tidal phase lag of Venus (Rosenblatt et al., 2021; Smrekar et al., 2022). These interior properties are directly related to the timescales of mantle convection, interior thermal state, and the size and number of mantle plumes. The gravity science investigation will also provide high-resolution gravity and topography measurements, which will enhance knowledge of crustal processes and deformation and provide precise estimates of elastic (or lithosphere) thickness (Rosenblatt et al., 2021; Smrekar et al., 2022). As shown in the methods of this work, lithosphere thickness is directly related to surface heat flux, so surface heat flux will be an indirectly obtainable parameter as well. The VERITAS and EnVision gravity science investigation will provide updated constraints on the interior structure (crustal and lithospheric thickness) and surface heat flux parameters that are used in the melt generation analytical model presented here. Additionally, the improved understanding on mantle convection processes and abundance of mantle plumes can be used to more accurately model convection-driven and plume-driven thinning or extension of the lithosphere.

InSAR will allow VERITAS to take high resolution imagery, topography measurements, and surface deformation measurements that may be changing over time. Changes in surface deformation may reflect subsurface magmatic processes in near-real time (Poland and Lu, 2008; Wicks et al., 2002), and so these measurements can be used in combination with measured gravity fields to estimate location, size, and depth of magma reservoirs. Characterizing the

distribution of magma in the crust or lithosphere will also have implications for melt production rates in the asthenosphere and magma flux into the lithosphere. The infrared spectrometers on VERITAS and EnVision will map surface composition on a global scale as well as observe thermal emissions continuously, of which anomalous thermal emissions likely reflect active volcanic eruptions (Helbert et al., 2018). The area of any observed thermal emission anomalies can be used to estimate eruptive volume and corresponding melt production rates. The InSAR and infrared spectrometer measurements will provide estimates for present-day global eruption rates, intrusive-to-extrusive ratios, and magma flux. These estimates can be compared to modeled outputs of melt production rate and inferred magma flux to determine which parameters best match the new observations.

While computational models, including the analytical model developed for this work, will need to be updated based on new constraints and findings provided by future missions, using these models now will provide end-members of what we can expect to observe during future missions. The model results presented here indicate that large-scale melting is possible under Venusian conditions over a broad range of parameters and driving mechanisms, supporting the hypotheses that Venus remains the only other volcanically active planet in our solar system, beyond Earth. While the exact values of melt area, melt production rate, and surface heat flux from this work may not be correct, these results provide estimates that are likely within an order of magnitude of real values and so provide new constraints on these parameters and associated parameters such as global eruptive volume and rate.

CHAPTER 5.

CONCLUSION

This work explores magmatic and interior processes that may still be active on Venus today. This will provide a better understanding of magmatic systems in volcano-tectonic settings, which could have implications for Venus' geodynamic regime, heat loss mechanisms, and active volcanism under conditions of the present and recent past. The results of this modeling will assist in interpreting geophysical data from future missions, particularly by providing reference surface heat flux, crustal/lithospheric thicknesses, and expected melt quantities at various stages of rift evolution. The modeled outputs of heat flux and crustal/lithospheric thicknesses can be directly compared to values for these parameters determined by upcoming missions: NASA's VERITAS and ESA's EnVision. Additionally, observations of new lava flows or volcanic edifices may allow for estimates of expected magma fluxes (melt production rates) and/or intrusive-extrusive ratios, which can be compared to the modeled outputs of generated melt area and melt production rate. These comparisons may indicate which modeled parameter set(s) (i.e., which combination(s) of model parameters) Venus is most similar to at present. Because of the abundance of volcanic activity across the solar system, the models developed in this work may also be applicable to geologic processes on other planetary bodies with single-plate tectonics (e.g., Mars, Mercury, the Moon, Io) as well as early Earth.

REFERENCES CITED

Airey, M. W., Mather, T. A., Pyle, D. M., & Ghail, R. C. (2017). The distribution of volcanism in the Beta-Atla-Themis region of Venus: Its relationship to rifting and implications for global tectonic regimes. *Journal of Geophysical Research: Planets*, *122*(8), 1626-1649. https://doi.org/10.1002/2016JE005205

Anderson, F. S. & Smrekar, S. E. (2006). Global mapping of crustal and lithospheric thickness on Venus. *J. Geophys. Res., Planets* 111(E8), E08006 https://doi.org/10.1029/2004JE002395

Basilevsky, A. T., et al. (2012), Geologic interpretation of the near-infrared images of the surface taken by the Venus Monitoring Camera, Venus Express, *Icarus*, 217(2), 434–450. https://doi.org/10.1016/j.icarus.2011.11.003

Basilevsky, A. T. (1993). Age of rifting and associated volcanism in Atla Regio, Venus. *Geophysical Research Letters*, *20*(10), 883–886. https://doi.org/10.1029/93GL00736

Bercovici, D. (2010). Mantle convection. *Encyclopedia of Solid Earth Geophysics*, 1-21.

Bjonnes, E. E., Hansen, V. L., James, B., & Swenson, J. B. (2012). Equilibrium resurfacing of Venus: Results from new Monte Carlo modeling and implications for Venus surface histories. *Icarus*, *217*(2), 451-461. https://doi.org/10.1016/j.icarus.2011.03.033

Bland, M. T., & Elder, C. M. (2022). Silicate volcanism on Europa's seafloor and implications for habitability. *Geophysical Research Letters*, 49, e2021GL096939. https://doi.org/10.1029/2021GL096939

Burov, E. & Cloetingh, S. (2009). Controls of mantle plumes and lithospheric folding on modes of intraplate continental tectonics: differences and similarities. *Geophys. J. Int.* 178, 1691–1722. https://doi.org/10.1111/j.1365-246X.2009.04238.x

Byrne, P. K., Ghail, R. C., Şengör, A. M. C., James, P. B., Klimczak, C., & Solomon, S. C. (2021). A globally fragmented and mobile lithosphere on Venus. *Proceedings of the National Academy of Sciences*, 118(26), e2025919118.
https://doi.org/10.1073/pnas.2025919118

Cawood, P.A., Hawkesworth, C.J., and Dhuime, B. (2012). The continental record and the generation of continental crust. *Geol Soc Am Bull* 125:14–32. https://doi.org/10.1130/b30722.1

Crisp, J.A. (1984). Rates of magma emplacement and volcanic output. *J Volcanol Geotherm Res* 20:177–211. https://doi.org/10.1016/0377-0273(84)90039-8

Cutler, K. S., Filiberto, J., Treiman, A. H., and Trang, D. (2020). Experimental investigation of oxidation of pyroxene and basalt: Implications for spectroscopic analyses of the surface of Venus and the ages of lava flows. *Planet. Sci. J.* 1.1: 21. https://doi.org/10.3847/PSJ/ab8faf

D'Incecco, P., Filiberto, J., López, I., Gorinov, D. A., and Komatsu, G. (2021). Idunn Mons: Evidence for Ongoing Volcano-tectonic Activity and Atmospheric Implications on Venus. *Planet. Sci. J.* 2.5: 215. https://doi.org/10.3847/PSJ/ac2258

D'Incecco, P., López, I., Komatsu, G., Ori, G.G., Aittola, M., 2020. Local stratigraphic relations at Sandel crater, Venus: possible evidence for recent volcano-tectonic activity in Imdr Regio. *Earth Planet. Sci. Lett.* 546, 116410. https://doi.org/10.1016/j.epsl.2020

Elkins-Tanton, L. T., Smrekar, S. E., Hess, P. C., & Parmentier, E. M. (2007). Volcanism and volatile recycling on a one-plate planet: Applications to Venus. *Journal of Geophysical Research: Planets*, *112*(E4). https://doi.org/10.1029/2006JE002793

Farnetani, C. G. (1997), Excess temperature of mantle plumes: The role of chemical stratification across D'', *Geophys. Res. Lett.*, 24, 1583–1586. https://doi.org/10.1029/97GL01548

Filiberto, J., Trang, D., Treiman, A. H., and Gilmore, M. S. (2020). Present-day volcanism on Venus as evidenced from weathering rates of olivine. *Sci. Adv.* 6, https://doi.org/10.1126/sciadv.aax7445

Gerya, T. V. (2014). Plume-induced crustal convection: 3D thermomechanical model and implications for the origin of novae and coronae on Venus. *Earth and Planetary Science Letters*, *391*, 183-192. https://doi.org/10.1016/j.epsl.2014.02.005

Ghail, R. C., Hall, D., Mason, P. J., Herrick, R. R., Carter, L. M., & Williams, E. (2018). VenSAR on EnVision: Taking earth observation radar to Venus. *International journal of applied earth observation and geoinformation*, *64*, 365-376. https://doi.org/10.1016/j.jag.2017.02.008

Ghail, R. (2015). Rheological and petrological implications for a stagnant lid regime on Venus. *Planetary and Space Science*, *113*, 2-9. https://doi.org/10.1016/j.pss.2015.02.005

Gmerek, A. T., Weller, M. B., Kiefer, W. S., & Gregg, T. K. P. (2024). Mapping and Analysis of Ganis Chasma Rift System, Atla Regio, Venus. *LPI Contributions*, *3040*, 1623.

Grimm, R.E. & Hess, P.C. (1997). The crust of Venus, in *Venus II*, ed. by S.W. Bougher et al. (University of Arizona Press, Tuscon, 1997), pp. 1205–1244.

Gülcher, A. J. P., Gerya, T. V., Montési, L. G. J. et al. (2020). Corona structures driven by plume–lithosphere interactions and evidence for ongoing plume activity on Venus. *Nat. Geosci.* 13, 547–554, https://doi.org/10.1038/s41561-020-0606-1

Guseva, E.N., Ivanov, M.A. Regional Geologic and Morphologic Characterization of Rift Zones on Venus. Sol Syst Res 53, 233–244 (2019). https://doi.org/10.1134/S003809461904004X

Hahn, R. M., & Byrne, P. K. (2023). A morphological and spatial analysis of volcanoes on Venus. *Journal of Geophysical Research: Planets*, *128*(4), e2023JE007753. https://doi.org/10.1029/2023JE007753

Havlin, C., Parmentier, E. M., & Hirth, G. (2013). Dike propagation driven by melt accumulation at the lithosphere–asthenosphere boundary. *Earth and Planetary Science Letters*, *376*, 20-28. https://doi.org/10.1016/j.epsl.2013.06.010

Helbert, J., Dyar, D., Walter, I., Wendler, D., Widemann, T., Marcq, E., ... & Smrekar, S. (2018, September). The Venus Emissivity Mapper (VEM): obtaining global mineralogy of Venus from orbit. In *Infrared remote sensing and instrumentation XXVI* (Vol. 10765, pp. 102-113). SPIE. https://doi.org/10.1117/12.2320112

Herrick, R. R., & Hensley, S. (2023). Surface changes observed on a Venusian volcano during the Magellan mission. *Science*, *379*(6638), 1205-1208. https://doi.org/10.1126/science.abm7735

Herrick, R. R., & Rumpf, M. E. (2011). Postimpact modification by volcanic or tectonic processes as the rule, not the exception, for Venusian craters. *Journal of Geophysical Research: Planets*, *116*(E2). https://doi.org/10.1029/2010JE003722

Ingersoll, A. P. (1969). The runaway greenhouse: A history of water on Venus. *Journal of Atmospheric Sciences*, *26*(6), 1191-1198. https://doi.org/10.1175/1520-0469(1969)026<1191:TRGAHO>2.0.CO;2

Ivanov, M. A. & Head. J. W. (2013). The history of volcanism on Venus. *Planetary and Space Science* 84, 66-92. https://doi.org/10.1016/j.pss.2013.04.018

Ivanov, M. and Head, J.W. (2010). Lada Terra rise and Quetzalpetlatl Corona: a region of long lived mantle upwelling and recent volcanic activity on Venus. *Planet. Space Sci.* 58, 1880–1894. https://doi.org/10.1016/j.pss.2010.08.018

James, P. B., Zuber, M. T., and Phillips, R. J. (2013). Crustal thickness and support of topography on Venus. *J. Geophys. Res.* 118, 859–875, https://doi.org/10.1029/2012JE004237

Jiménez-Díaz, A., Ruiz, J., Kirby, J. F., Romeo, I., Tejero, R., and Capote, R. (2015). Lithospheric structure of Venus from gravity and topography. *Icarus* 260, 215–231. https://doi.org/10.1016/j.icarus.2015.07.020

Kasting, J. (1988). Runaway and moist greenhouse atmospheres and the evolution of Earth and Venus. *Icarus*, 74, 472–494. https://doi.org/10.1016/0019-1035(88)90116-9

Katz, R. F., Spiegelman, M., & Langmuir, C. H. (2003). A new parameterization of hydrous mantle melting. *Geochemistry, Geophysics, Geosystems*, *4*(9). https://doi.org/10.1029/2002GC000433

Le Feuvre, M., & Wieczorek, M. A. (2011). Nonuniform cratering of the Moon and a revised crater chronology of the inner Solar System. *Icarus*, *214*(1), 1-20. https://doi.org/10.1016/j.icarus.2011.03.010

López, I., D'Incecco, P., Filiberto, J., & Komatsu, G. (2022). The volcanology of Idunn Mons, Venus: The complex evolution of a possible active volcano. *Journal of Volcanology and Geothermal Research*, *421*, 107428. https://doi.org/10.1016/j.jvolgeores.2021.107428

Lourenço DL, Rozel AB, Gerya T, Tackley PJ (2018) Efficient cooling of rocky planets by intrusive magmatism. *Nature Geoscience* 11:322–327. https://doi.org/10.1038/s41561-018-0094-8

Lourenço DL, Rozel AB, Ballmer MD, Tackley PJ (2020) Plutonic-squishy lid: a new global tectonic regime generated by intrusive magmatism on Earth-like planets. *Geochem Geophys Geosyst*, 21:e2019GC008756. https://doi.org/10.1029/2019gc008756

Magee, K. P., & Head, J. W. (1995). The role of rifting in the generation of melt: Implications for the origin and evolution of the Lada Terra-Lavinia Planitia region of Venus. *Journal of Geophysical Research: Planets*, *100*(E1), 1527-1552. https://doi.org/10.1029/94JE02334

Margot, J. L., Campbell, D. B., Giorgini, J. D., Jao, J. S., Snedeker, L. G., Ghigo, F. D., & Bonsall, A. (2021). Spin state and moment of inertia of Venus. *Nature Astronomy*, *5*(7), 676-683. https://doi.org/10.1038/s41550-021-01339-7

Masursky, H., Eliason, E., Ford, P. G., McGill, G. E., Pettengill, G. H., Schaber, G. G., & Schubert, G. (1980). Pioneer Venus radar results: Geology from images and altimetry. Journal of Geophysical Research, 85(A13), 8232–8260. https://doi.org/10.1029/JA085iA13p08232

McGill, G. E., Steenstrup, S. J., Barton, C., and Ford, P. G., (1981). Continental rifting and the origin of Beta-Regio, Venus. *Geophys. Res. Lett.* ***8***, 737. https://doi.org/10.1029/GL008i007p00737

Mulyukova, E., & Bercovici, D. (2020). Mantle convection in terrestrial planets. In *Oxford Research Encyclopedia of Planetary Science*. https://doi.org/10.1093/acrefore/9780190647926.013.109

Nakagawa, T. & Tackley, P.J. (2012). Influence of magmatism on mantle cooling, surface heat flow and Urey ratio. *Earth Planet. Sci. Lett.* 329–330, 1–10. https://doi.org/10.1016/j.epsl.2012.02.011

O'Rourke, J. G., & Smrekar, S. E. (2018). Signatures of lithospheric flexure and elevated heat flow in stereo topography at coronae on Venus. *Journal of Geophysical Research: Planets*, *123*(2), 369-389. https://doi.org/10.1002/2017JE005358

Phillips, R. J., Raubertas, R. F., Arvidson, R. E., Sarkar, I. C., Herrick, R. R., Izenberg, N., & Grimm, R. E. (1992). Impact craters and Venus resurfacing history. *Journal of Geophysical Research: Planets*, *97*(E10), 15923-15948. https://doi.org/10.1029/92JE01696

Phillips, R. J. (1990). Convection-driven tectonics on Venus. *Journal of Geophysical Research: Solid Earth*, *95*(B2), 1301-1316. https://doi.org/10.1029/JB095iB02p01301

Phillips, R. J. & Malin, M. C., (1984). Tectonics of Venus. *Annu. Rev. Earth Planet. Sci.* ***12***, 411. https://doi.org/10.1146/annurev.ea.12.050184.002211

Poland, M. P. & Lu, Z. (2008). Radar interferometry observations of surface displacements during pre-and coeruptive periods at Mount St. Helens, Washington, 1992–2005. US geological survey professional paper, 1750, 361-382.

Roberts, K. & Head, J. W. (1993). Large scale volcanism associated with coronae on Venus: implications for formation and evolution. *Geophys. Res. Lett.* **20**, 1111–1114. https://doi.org/10.1029/93GL01484

Rolf, T., Weller, M., Gülcher, A. *et al.* (2022). Dynamics and Evolution of Venus' Mantle Through Time. *Space Sci Rev* **218**, 70. https://doi.org/10.1007/s11214-022-00937-9

Romeo, I., & Turcotte, D. L. (2010). Resurfacing on venus. *Planetary and Space Science*, *58*(10), 1374-1380. https://doi.org/10.1016/j.pss.2010.05.022

Rosenblatt, P., Dumoulin, C., Marty, J. C., & Genova, A. (2021). Determination of Venus' interior structure with EnVision. *Remote Sensing*, *13*(9), 1624. https://doi.org/10.3390/rs13091624

Ruiz, J., Jiménez-Díaz, A., Egea-González, I., Romeo, I., Kirby, J. F., & Audet, P. (2024). Heat loss and internal dynamics of Venus from global surface heat flow estimates. *arXiv preprint arXiv:2401.06558*.

Russell, M. B., & Johnson, C. L. (2021). Evidence for a locally thinned lithosphere associated with recent volcanism at Aramaiti Corona, Venus. *Journal of Geophysical Research: Planets*, *126*(8), e2020JE006783. https://doi.org/10.1029/2020JE006783

Schaber, G. G. (1982). Venus: Limited extension and volcanism along zones of lithospheric weakness. *Geophysical Research Letters*, 9(5), 499–502. https://doi.org/10.1029/GL009i005p00499

Schilling, J.-G. (1991), Fluxes and excess temperatures of mantle plumes inferred from their interaction with migrating midocean ridges, *Nature*, 352, 397–403. https://doi.org/10.1038/352397a0

Schubert, G. (1997). Mantle convection. In: *Encyclopedia of Planetary Science. Encyclopedia of Earth Science*. Springer, Dordrecht. https://doi.org/10.1007/1-4020-4520-4_233

Shalygin, E. V., Markiewicz, W. J., Basilevsky, A. T., Titov, D. V., Ignatiev, N. I., and Head, J. W. (2015). Active volcanism on Venus in the Ganiki Chasma rift zone. *Geophys. Res. Lett*., https://doi.org/10.1002/2015GL064088

Smrekar, S., Hensley, S., Nybakken, R., Wallace, M. S., Perkovic-Martin, D., You, T. H., ... & Mazarico, E. (2022, March). VERITAS (Venus emissivity, radio science, InSAR, topography, and spectroscopy): a discovery mission. In *2022 IEEE aerospace conference (AERO)* (pp. 1-20). IEEE. 10.1109/AERO53065.2022.9843269

Smrekar, S.E., Davaille, A. & Sotin, C. (2018). Venus Interior Structure and Dynamics. *Space Sci. Rev*., 214, 88. https://doi.org/10.1007/s11214-018-0518-1

Smrekar, S.E., Stofan, E.R., Mueller, N., Treiman, A., Elkins-Tanton, L., Helbert, J., Piccioni, G., and Drossart, P. (2010). Recent Hotspot Volcanism on Venus from VIRTIS emissivity data. *Science* 328, 605–608. DOI:10.1126/science.1186785

Solomatov, V. S., & Moresi, L. N. (1996). Stagnant lid convection on Venus. *Journal of Geophysical Research: Planets*, *101*(E2), 4737-4753. https://doi.org/10.1029/95JE03361

Solomon, S. C., Smrekar, S. E., Bindschadler, D. L., Grimm, R. E., Kaula, W. M., McGill, G. E., ... & Stofan, E. R. (1992). Venus tectonics: An overview of Magellan observations. *Journal of Geophysical Research: Planets*, *97*(E8), 13199-13255. https://doi.org/10.1029/92JE01418

Solomon, S. C., & Head, J. W. (1982). Mechanisms for lithospheric heat transport on Venus: Implications for tectonic style and volcanism. *Journal of Geophysical Research: Solid Earth*, *87*(B11), 9236-9246. https://doi.org/10.1029/JB087iB11p09236

Stacey, F.D. (2007). Mantle, Thermal Conductivity. In: Gubbins, D., Herrero-Bervera, E. (eds) *Encyclopedia of Geomagnetism and Paleomagnetism*. Springer, Dordrecht. (p. 688-689). https://doi.org/10.1007/978-1-4020-4423-6_213

Stoddard, P. R., & Jurdy, D. M. (2012). Topographic comparisons of uplift features on Venus and Earth: Implications for Venus tectonics. *Icarus*, *217*(2), 524-533. https://doi.org/10.1016/j.icarus.2011.09.003

Stofan, E. R., Smrekar, S. E., Tapper, S. W., Guest, J. E., & Grindrod, P. M. (2001). Preliminary analysis of an expanded corona database for Venus. *Geophysical Research Letters*, *28*(22), 4267-4270. https://doi.org/10.1029/2001GL013307

Stofan, E. R., Smrekar, S. E., Bindschadler, D. L., and Senske, D., (1995). Large topographic rises on Venus: Implications for mantle upwellings. *J. Geophys. Res.* ***23***, 317. https://doi.org/10.1029/95JE01834

Strom, R., Schaber, G., and Dawson, D. (1994). The global resurfacing of Venus. *J. Geophys. Res.* 99, 10,899–10,926. https://doi.org/10.1029/94JE00388

Treiman, A. H., (2007). Geochemistry of Venus' surface: current limitations as future opportunities. In: Esposito, L.W., Stofan, E.R., Cravens, E. (Eds.), Exploring Venus as a Terrestrial Planet: Geophysical Monograph, vol. 176. American Geophysical Union, Washington, DC.

Trønnes, R. G., Baron, M. A., Eigenmann, K. R., Guren, M. G., Heyn, B. H., Løken, A., & Mohn, C. E. (2019). Core formation, mantle differentiation and core-mantle interaction within Earth and the terrestrial planets. *Tectonophysics*, *760*, 165-198. https://doi.org/10.1016/j.tecto.2018.10.021

Turcotte, D. L. (1989). A heat pipe mechanism for volcanism and tectonics on Venus. *Journal of Geophysical Research: Solid Earth*, *94*(B3), 2779-2785. https://doi.org/10.1029/JB094iB03p02779

Wicks, C.W., Dzurisin, D., Ingebritsen, S., Thatcher, W., Lu, Z. & Iverson, J. (2002). Magmatic activity beneath the quiescent Three Sisters volcanic center, central Oregon Cascade Range, USA. *Geophysical Research Letters*, 29 (7), 1122. https://doi.org/10.1029/2001GL014205

Zhong, S. (2006), Constraints on thermochemical convection of the mantle from plume heat flux, plume excess temperature, and upper mantle temperature, *J. Geophys. Res.*, 111, B04409, doi:10.1029/2005JB003972